J Mar Sci Technol (2009) 14:137–160
DOI 10.1007/s00773-009-0056-3

ORIGINAL ARTICLE

Database of sail shapes versus sail performance and validation of numerical calculations for the upwind condition

Yutaka Masuyama · Yusuke Tahara · Toichi Fukasawa · Naotoshi Maeda

Received: 31 March 2007 / Accepted: 17 March 2009 / Published online: 11 June 2009

Abstract A database of full-scale three-dimensional sail shapes is presented with the aerodynamic coefficients for the upwind condition of International Measurement System (IMS) type sails. Three-dimensional shape data are used for the input of numerical calculations and the results are compared with the measured sail performance. The sail shapes and performance were measured using sail dynamometer boat *Fujin*. This is a boat of 10.3-m length overall in which load cells and CCD cameras were installed to simultaneously measure the sail forces and shapes. At the same time, the sailing conditions of the boat, e.g., boat speed, heel angle, wind speed, and wind angle, were measured. The sail configurations tested were: mainsail with 130% jib, mainsail with 75% jib, and mainsail alone. Sail shapes were measured at several vertical positions for the shape parameters defined by: chord length, maximum draft, maximum draft position, entry angle at the luff, and exit angle at the leech, all of which finally yield three-dimensional coordinates of the sail geometry. The tabulated shape data, along with aerodynamic coefficients, are presented in this article. In addition, numerical flow simulations were performed for the measured sail shapes and the sailing conditions to investigate the capability and limitations of the methods through detailed comparison with the measurements. Two numerical methods were used: a vortex lattice method (VLM) and a Reynolds-averaged Navier–Stokes (RANS)-based computational fluid dynamics method. The sail shape database, in association with the numerical results, provides a good benchmark for the sail performance analysis of the upwind condition of IMS type sails.

Keywords Database · Sail shape · Sail performance · Validation · Vortex lattice method · RANS-based CFD

List of symbols

C_L, C_D	Lift force and drag force coefficients (−)
C_X, C_Y	Thrust force and side force coefficients (−)
C_{Dp}	Viscosity and parasitic drag coefficient of sail and rig (−)
S_A	Sail area (m^2)
U_A	Apparent wind speed (AWS) (m/s)
V_B	Boat velocity (m/s)
X, Y	Force components along x and y-axis in body axes system (N)
K, N	Moments around x and z-axis in body axes system (Nm)
x_{CE}, z_{CE}	x and z coordinates of the center of effort of the sails (m)
γ_A	Apparent wind angle (AWA) (°)
ρ_a	Density of air (kg/m^3)

1 Introduction

Because the recent advances in computational fluid dynamics (CFD) further motivate the application of numerical simulations to predict sail performance, there is

Y. Masuyama (✉) · T. Fukasawa
Kanazawa Institute of Technology, 7-1 Ohgigaoka, Nonoichi, Ishikawa 921-8501, Japan
e-mail: masuyama@neptune.kanazawa-it.ac.jp

Y. Tahara
National Maritime Research Institute, Japan, 6-38-1 Shinkawa, Mitaka, Tokyo 181-0004, Japan

N. Maeda
Daihatsu Motor Co., Ltd., Ikeda, Osaka 563-0044, Japan

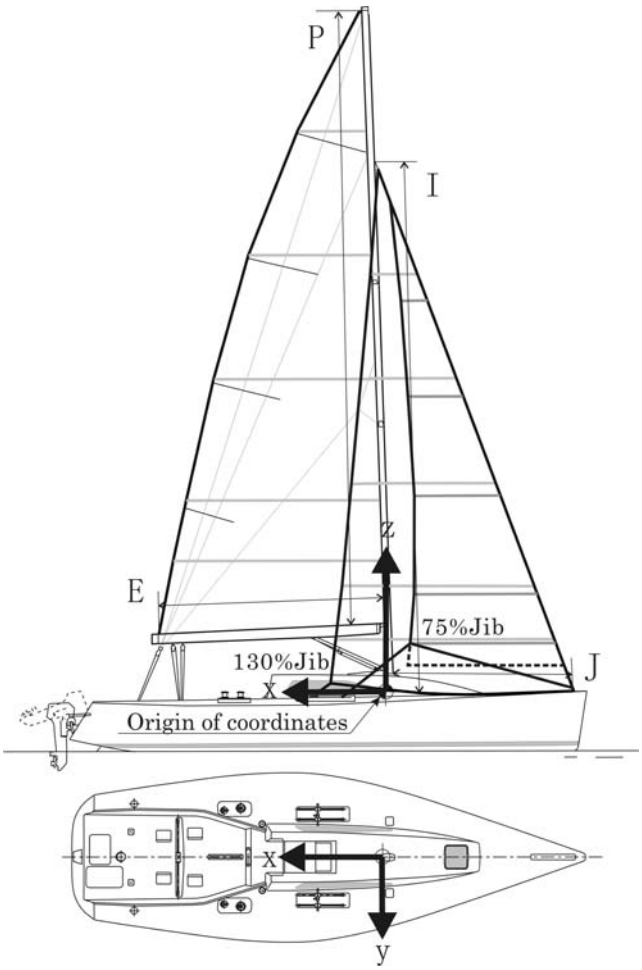

Fig. 1 Schematic showing the sail plan of *Fujin* with a 130% jib and a 75% jib and the coordinate system

Table 1 Principal dimensions of *Fujin*

HULL	
Length over all (m)	10.35
Length of water line (m)	8.80
Maximum breadth (m)	3.37
Breadth of water line (m)	2.64
Disp (ton)	3.86
SAIL	
I (m)	11.00
J (m)	3.61
P (m)	12.55
E (m)	4.51

Table 2 Detailed measurements of sails

	Mainsail	130% Jib	75% Jib
Peak height (m)	13.82	10.70	9.90
Luff length (m)	12.50	11.45	10.60
Foot length (m)	4.44	4.89	3.16[a]
Sail area (m^2)	33.20	26.10	13.70
Height (%)	Chord length (m)		
0	4.44	4.89	0.00
10	4.13	4.44	2.90
20	3.85	3.94	2.45
40	3.23	2.94	1.70
60	2.43	1.97	1.06
80	1.39	0.98	0.53
100	0.15	0.10	0.10

[a] Foot length of 75% jib indicates value at 5% height

an ever increased need for reliable experimental data for validation. In general, such experiments are extremely complex and consequently very expensive to conduct because the simultaneous measurement of sail forces, sail shapes, and wind conditions is required. Wind tunnel tests can be performed relatively easily, but scale effects related both to flow and structural aspects, which yield inaccuracy in sail shape measurements, are always present. Full-scale onboard measurements are free from scale-effect problems and appear more promising, but the challenge becomes how to accurately measure the forces acting on the sail. Such studies on sail force measurements have been performed by [1, 2], and [3], who built full-scale boats with onboard sail dynamometer systems.

Milgram et al. [1] showed in his pioneering work that the sail dynamometer boat *Amphetrete* was quite effective. This measurement system consists of a 10.7-m boat with an internal frame connected to the hull by six load cells that were configured to measure all forces and moments acting on the sails. In his work, the sail shapes were also measured and used for CFD analyses; however, unfortunately, details of the sail shape and performance data were not presented.

Hochkirch and Brandt [3] also built a 10.1-m dynamometer boat DYNA. The aerodynamic forces acting on the sail were measured and compared with the results from wind tunnel tests [4]. The measured data were also used as input to a CFD calculation, and a parametric survey was carried out [5]. However, this work does not provide a database for the relation between sail shape and performance.

Masuyama and Fukasawa [2, 6] were encouraged by Milgram's work, and built the sail dynamometer boat *Fujin*. The *Fujin* is a 10.3-m sailing cruiser in which load cells, CCD cameras, and a sailing condition measurement system are installed to obtain the sail forces and shapes and the boat attitude simultaneously. The measurement system installed in the *Fujin* and the results of calibration tests and sailing tests have already been reported [2, 6]. These will be referred to below as the previous articles. In these articles the sail performance variation was indicated with

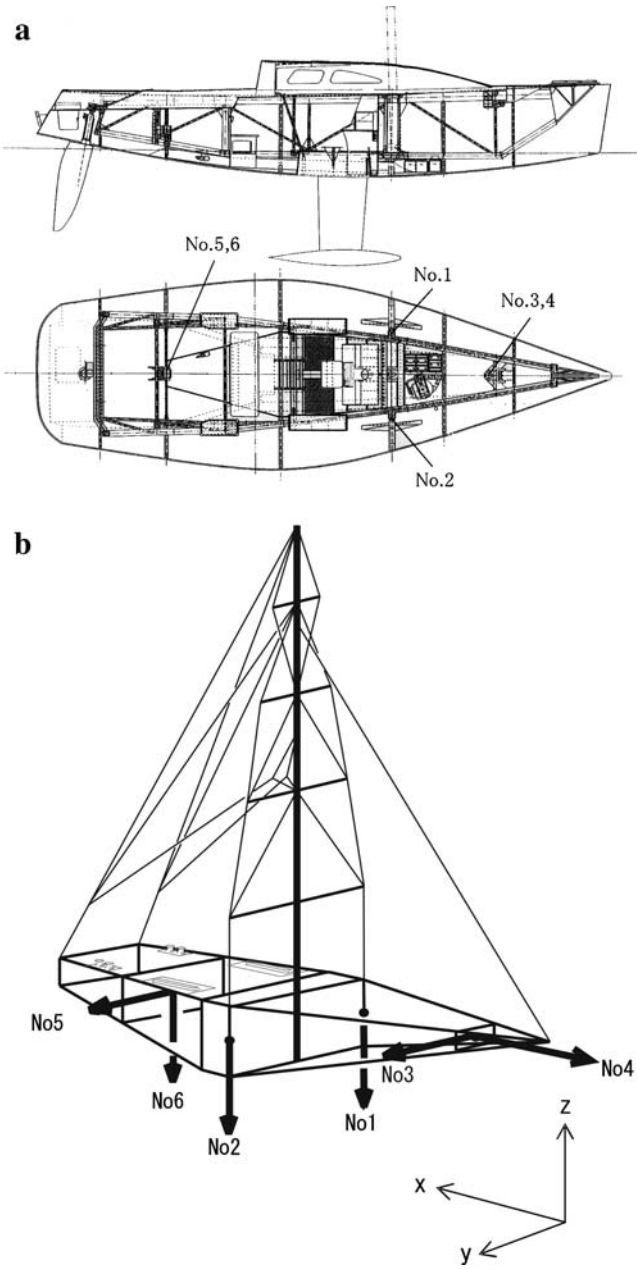

Fig. 2 **a** General arrangement of the dynamometer frame in *Fujin*. **b** Directions of the measured components of each load cell of the dynamometer frame. *1–6* indicate the components measured by the load cells

the change of apparent wind angle and mainsail draft. Numerical calculations using the vortex lattice method (VLM) developed by Fukasawa [7] were also performed using the measured sail shape.

In this article, the relationship between the sail shape and the performance for the upwind condition is presented, and the results are compared with those of the latest numerical calculation methods. Also included are the

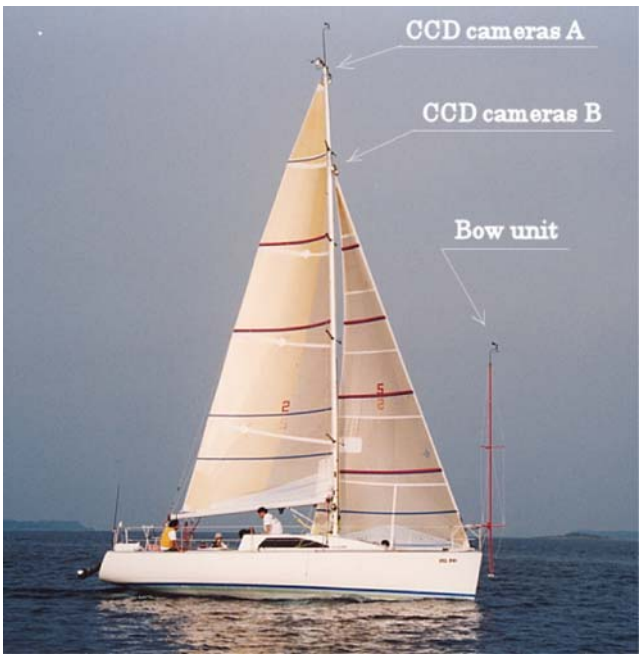

Fig. 3 Sea trial condition in light wind with 130% jib. *A* and *B* indicate pairs of cameras for viewing the lower parts of the main sail and jib. An anemometer attached to the bow unit measured the apparent wind speed and apparent wind angle

results obtained from experiments performed since the previous articles were published.

A Reynolds-averaged Navier–Stokes (RANS)-based CFD method developed by Tahara (FLOWPACK version 2005) was used to demonstrate validation of the method through detailed comparison with the present measurements. Detailed validation studies of the method have been conducted for transition of the method to the industrial design field through application to geometries and flows which are theoretically and/or experimentally well understood and/or are well-known test cases. For instance, Tahara [8–10], Tahara and Ando [11] and Tahara et al. [12] are related to the evaluation of the accuracy of predicting ship viscous free-surface flow and propulsive performance, and Tahara et al. [13, 14] also address CFD-based ship-hull-form optimizations. In addition, several extended applications were investigated, e.g., the multiple sail design for an America's Cup sailing boat [15] and the parachute design for a spacecraft landing on Mars [16].

In fact, the present application of the RANS-based CFD method to sail flow calculations is a new challenge for CFD. The pros and cons of the approach in comparison to the well-established potential-flow technique will be clarified. The authors believe that the results from the present validation exercise increases the motivation to further enhance CFD technology. To do this will involve a more detailed analysis of the sail flow, as carried out in the present study.

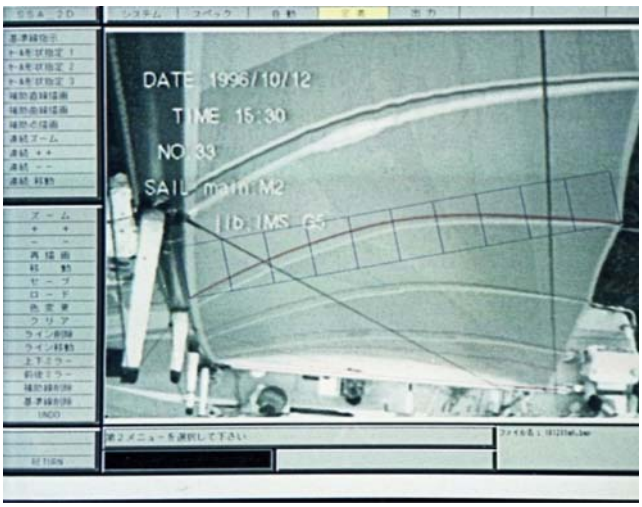

Fig. 4 Example of a processed image of the mainsail using sail shape analysis software SSA-2D

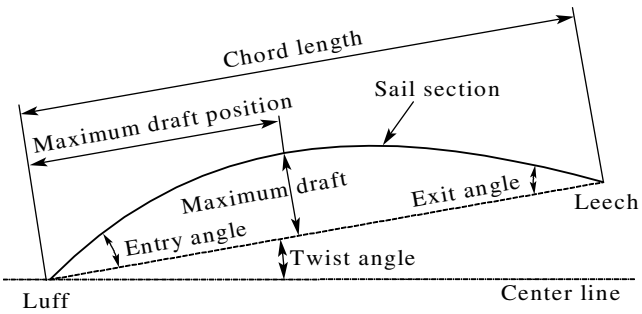

Fig. 5 Measured sail shape parameters

2 Sail plan and definition of coefficients

Full-scale sail tests were performed using the sail dynamometer boat *Fujin*. The *Fujin* was originally built for conducting tests on sails for the Japanese America's Cup entry in 1994. *Fujin* is a 10.3-m-long ocean cruiser with a sail dynamometer system in the hull that can directly measure sail forces and moments. Figure 1 shows the general arrangement of the *Fujin*.

The test sails were made to correspond to a typical sail plan for an International Measurement System (IMS) class boat. The rigging of the *Fujin* was originally designed for testing sails for an International America's Cup Class (IACC) boat. The jib of an IACC boat is relatively small. Therefore, the longitudinal position of the jib rail track of the *Fujin* was located further forward than that of a typical IMS boat. For this reason, the tests were performed using either a 130% jib or a 75% jib and a fully batten mainsail. The sails were made by North Sails Japan. Table 1 shows the principal dimensions of the boat and sail, where I, J, P, and E are the measurement lengths of sail dimensions according to the IMS rules as defined in Fig. 1. Table 2 shows the detailed measurements of the sails. The 75% jib has a cut up foot as shown in Fig. 1. In order to apply the automatic gridding scheme for the numerical calculation, the foot shape was replaced by the dotted line shown in the diagram.

The coordinate system is also shown in Fig. 1. The origin is located on the vessel's centerline (y-direction) at the aft face of the mast (x-direction), and the height of deck level at the base of the forestay (z-direction). The aerodynamic coefficients and the coordinates of the center of effort of the sails are defined as follows:

$$C_X = \frac{X_S}{\frac{1}{2}\rho_a U_A^2 S_A}, \quad C_Y = \frac{Y_S}{\frac{1}{2}\rho_a U_A^2 S_A}, \quad x_{CE} = \frac{N_S}{Y_S}, \quad z_{CE} = \frac{K_S}{Y_S} \tag{1}$$

where X_S and Y_S are the force components along the x and y axes of the boat, respectively, and K_S and N_S are the moments around the x and z axes. x_{CE} and z_{CE} are the x and z coordinates of the center of effort of the sails (CE). The thrust force coefficient C_X is expressed as positive for the forward direction and the side force coefficient C_Y is positive for both port and starboard directions. It should be noted that the coordinates are given in the body axis system. Therefore, when the boat heels, the Y_S force component is not in the horizontal plane but is normal to the mast. The aerodynamic forces acting on the mast and rigging are included in the measured sail forces.

3 Measurements of full-scale sail performance and sail shape

3.1 Sail dynamometer boat *Fujin*

The design of the *Fujin* is based on the YR-10.3-m class, which is an IMS ocean racer designed by Yamaha Motor Co. Ltd. Although the hull was made using a mold of that class, the deck and interior of the boat were modified to permit installation of the dynamometer frame.

3.2 Measurement system for the aerodynamic performance

The sail dynamometer system is composed of a rigid aluminum frame and the measured force components are numbered in the Fig. 2. The frame is separated structurally from the hull and connected to it by the load cells. The general arrangement of the dynamometer frame is given in Fig. 2a. The load cells are numbered in the figure. Two of

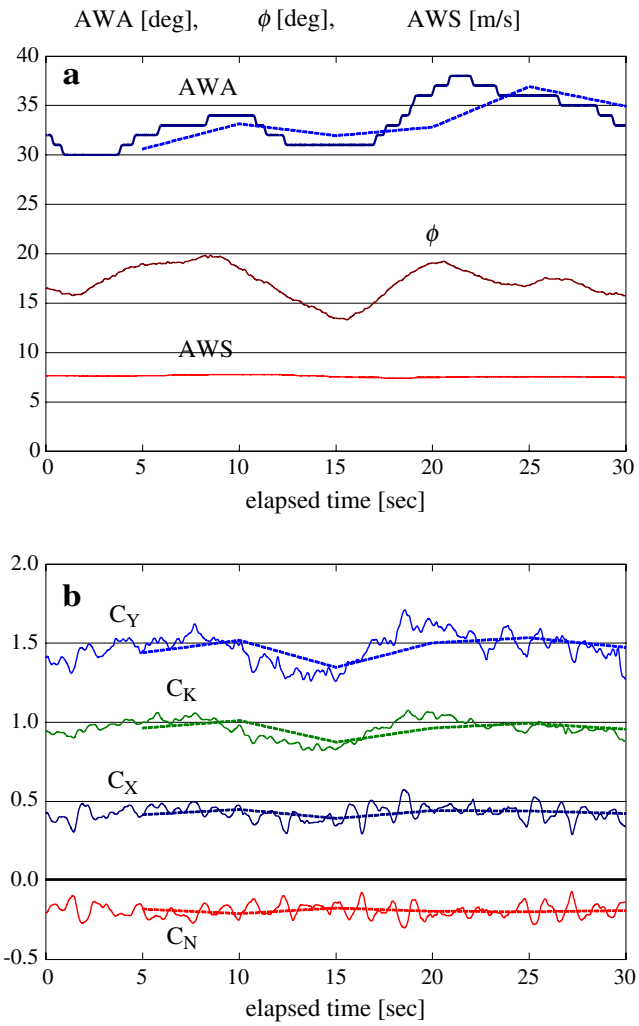

Fig. 6 Example of measured **a** apparent wind angle (*AWA*), apparent wind speed (*AWS*), heel angle (ϕ), and **b** aerodynamic coefficients (C_Y, side force coefficient; C_X, thrust force coefficient; C_K, heel moment coefficient; C_N, yaw moment coefficient) during 30 s recorded simultaneously at 10 Hz (for the case of a relatively large variation in AWA)

these are one-component load cells and the others are two-component cells.

The directions in which the loads were measured for each of the load cells are shown in Fig. 2b. Hence, these load cells form a six-component dynamometer system, and their outputs can be transformed to the forces and moments about the boat axes using a calibration matrix. All rig components such as the mast, chain plates, winches, and lead blocks were attached to the aluminum frame. The under-deck portion of the mast was held by the frame, and the other rig components were attached to the frame through deck holes. The data acquisition system and calibration method for the *Fujin* were described in previous articles [2, 6].

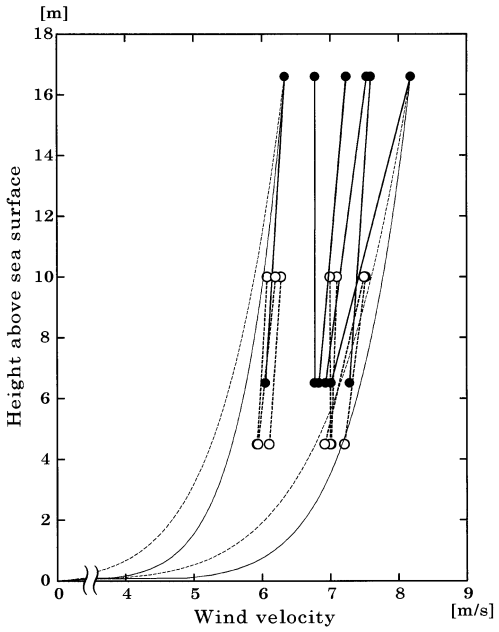

Fig. 7 Variation in wind velocity as a function of height above the sea surface in the testing area measured on the *Fujin* without sails. *Solid circles* indicate data measured at the mast top and bow unit; *open circles* indicate data measured by anemometers attached to the No. 1 spreader and the No. 3 spreader. Two *circles* connected by a *solid line* or a *dotted line* show data measured simultaneously. The *solid curves* show a 1/10 power curve and the *dotted curves* show a 1/7 power curve for reference

3.3 Measurement system for the sail shape and others

The sail shape was recorded using pairs of CCD cameras. The lower part of the mainsail was photographed using the CCD camera pair designated A in Fig. 3. These were located at the mast top, 50 cm transversely from each side of the mast. The upper part of the mainsail was photographed using a portable video camera from below the boom. The lower part of the jib was photographed using the camera pair designated B in Fig. 3, which were located at the intersection point of the forestay and the mast, 10 cm transversely from each side of the mast. The upper part of the jib was photographed using a portable video camera from inside the bow hatch. For measuring convenience, horizontal stripes were drawn on the mainsail and jib at heights of 10, 20, 40, 60 and 80% of each sail. The sail shape images were analyzed using the sail shape analyzing software SSA-2D, developed by Armonicos, Hamamatsu, Japan. Figure 4 shows an example of processed image of the mainsail using the SSA-2D. This software calculates the curvature of the sail section by marking several points of the sail stripe and the reference line on the PC display, and indicates the parameters such as chord length, maximum draft, maximum draft position, entry angle at the luff (leading edge), and exit angle at the leech (trailing edge), as shown in Fig. 5.

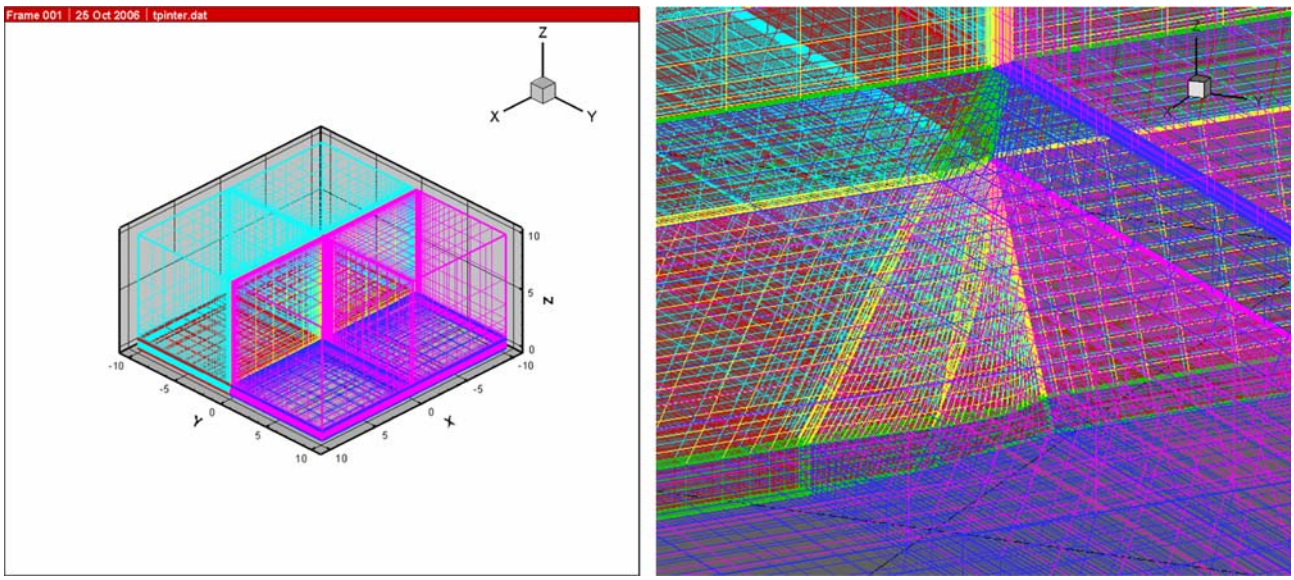

Fig. 8 Overview of the computational grid. The present automatic gridding scheme was used; the total number of grids was around half a million and the number of multiblocks was 48

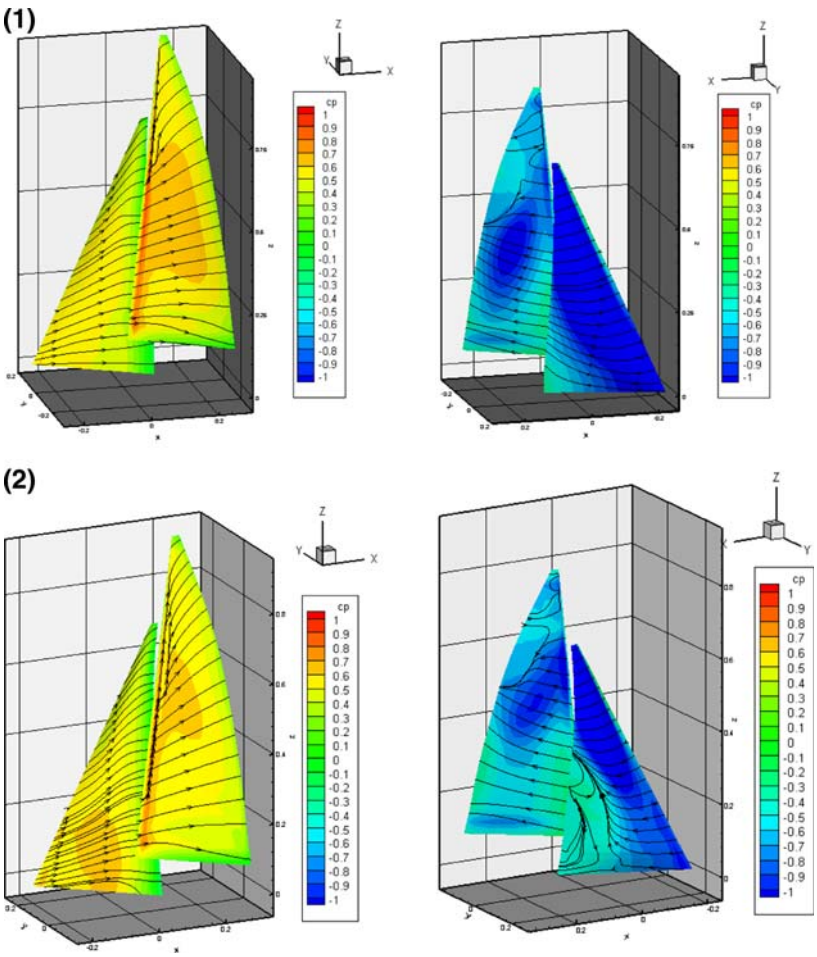

Fig. 10 (1) Surface pressure and streamlines obtained by RANS-based CFD for experimental ID 96092335 (AWA = 30.7°). (2) Surface pressure and streamlines obtained by RANS-based CFD at experimental ID 96080248 (AWA = 37.9°). The *left* and *right* diagrams correspond to the port and starboard sides, i.e., the pressure and suction sides, respectively

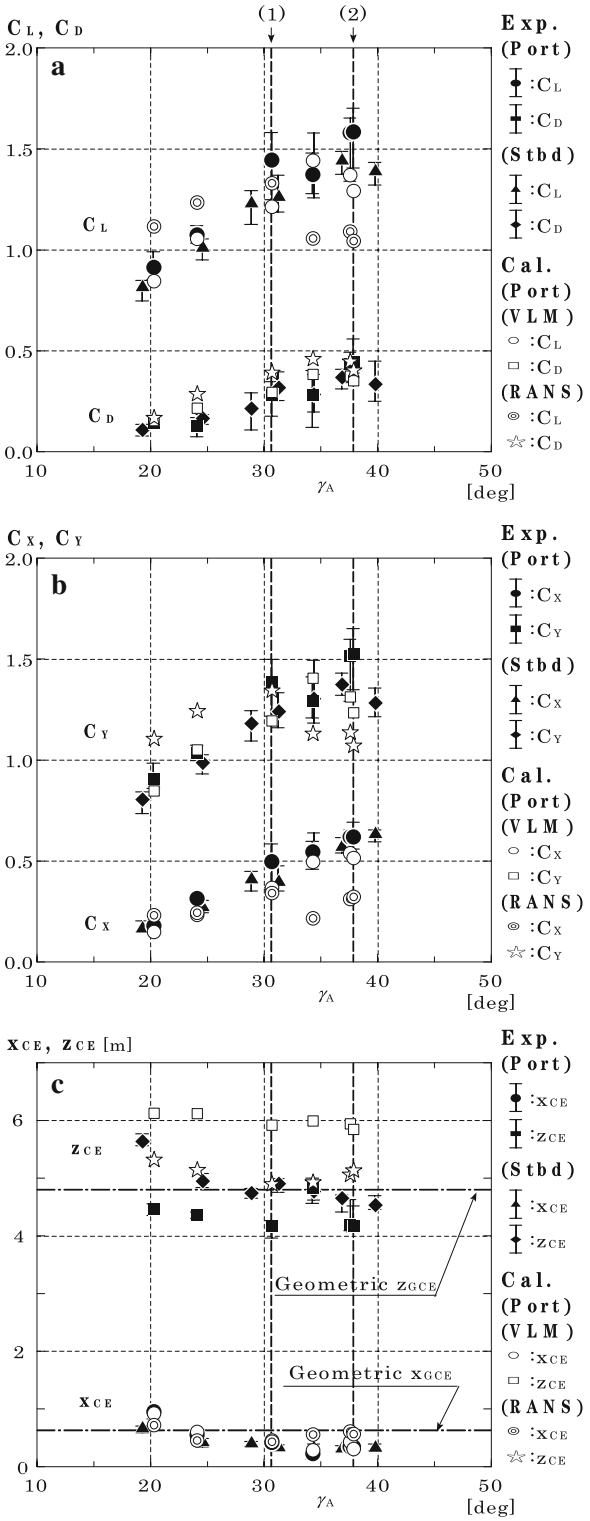

Fig. 9 Performance variation as a function of apparent wind angle (γ_A) for mainsail and 130% jib. **a** C_L, lift force coefficient; C_D, drag force coefficient; **b** C_X, thrust force coefficient; C_Y, side force coefficient; **c** x_{CE}, z_{CE}, x and z coordinates of the center of effort of the sails. *Exp* experimental results; *Cal* calculated results; *Stbd* starboard; *VLM* vortex lattice method; *RANS* Reynolds-averaged Navier–Stokes. *1* and *2* indicate the conditions in the associated tables

The twist angle of the lower part of the sail measured from the upper camera is determined by taking the angle from the centerline of the boat as the reference. In contrast, the twist angle of the upper part measured from the lower camera might not be correct due to lack of a reference line. Therefore, these twist angles were calibrated using the twist angle at 40% height, which coincided with the measured angle from the upper camera. In the previous articles [2, 6], the calibration of the twist angle of the upper part was not adequate. Hence all the measured sail shape data were reanalyzed for this report. From these data, three-dimensional coordinates of the sails were calculated by interpolation using spline curves.

The apparent wind speed (AWS) and apparent wind angle (AWA) were measured by an anemometer attached on the bow unit as shown in Fig. 3. This unit comprises a post that can rotate freely to maintain its vertical attitude when the boat heels in order to measure the wind data in the horizontal plane. The height of the anemometer coincides with the geometric center of effort (GCE) of the sail plan. The wind speed and wind angle sensors were calibrated using wind tunnel tests in advance and the calibration equations were obtained.

The *Fujin* also has motion measuring instruments such as an optical fiber gyroscope (roll and pitch angles), a flux gate compass (heading angle), a differential type GPS receiver, a speedometer (velocity in the x direction), and a potentiometer for the rudder angle. These data were recorded by an onboard computer simultaneously with the data from the load cells.

3.4 Test condition and error analysis

The sea tests were performed in Nanao Bay off the Noto Peninsula. The bay is approximately eight nautical miles from east to west and five from north to south. The bay is surrounded by low hills, and the mouth connecting it to the Japan Sea is narrow. Therefore, there is little tidal current in the bay and the wave heights are relatively small, even though the wind can be strong.

Close-hauled tests were conducted over an AWA range of 20°–40° and an AWS range of 5–11 m/s. The effect of the AWA and the draft and twist of the mainsail on the sail performance were measured.

Data sampling was started when the sailing condition was considered to be in steady state. The sampling rate for the data acquisition system was set at 10 Hz. Data sampling was continued for 90 s, and during this time the sail shapes were recorded using the CCD cameras. The steady state values were obtained by averaging the data over a 30- to 60-s period within the total measurement period of 90 s. This is because it took 90 s to record the sail shapes

Table 3 Sail shapes, measured experimental data and three-dimensional coordinates of the sails for the cases of (1) 96092335 and (2) 96080248

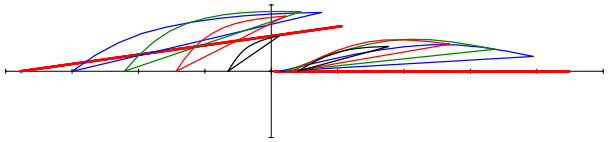

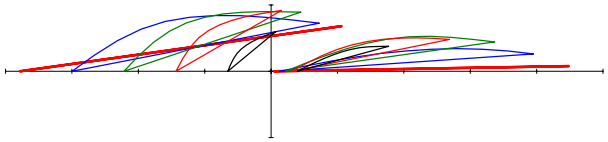

(1) 96092335

AWA[deg]	TWIST[deg]	DRAFT[%]	AWS[m/s]	HEEL[deg]	VB [kt]
30.7	15.5	8.6	6.9	15.1	5.0
C_L	C_D	C_X	C_Y	x_{CE} [m]	z_{CE} [m]
1.44	0.28	0.50	1.39	0.41	4.17

% of heit	130%Jib x	130%Jib y	130%Jib z	Mainsail x	Mainsail y	Mainsail z
	– 3.780	0.000	0.000	0.046	0.000	1.320
	– 2.812	0.136	0.000	0.934	0.000	1.320
0	– 1.843	0.272	0.000	1.822	0.000	1.320
%	– 0.875	0.408	0.000	2.710	0.000	1.320
	0.094	0.544	0.000	3.598	0.000	1.320
	1.062	0.681	0.000	4.486	0.000	1.320
	– 2.998	0.000	2.140	0.133	0.000	3.820
	– 2.305	0.429	2.140	0.888	0.176	3.820
20	– 1.568	0.667	2.140	1.645	0.322	3.820
%	– 0.805	0.795	2.140	2.406	0.400	3.820
	– 0.027	0.861	2.140	3.173	0.363	3.820
	0.760	0.886	2.140	3.947	0.222	3.820
	– 2.215	0.000	4.280	0.221	0.000	6.320
	– 1.771	0.442	4.280	0.834	0.227	6.320
40	– 1.272	0.719	4.280	1.452	0.405	6.320
%	– 0.723	0.850	4.280	2.081	0.483	6.320
	– 0.145	0.898	4.280	2.722	0.442	6.320
	0.448	0.898	4.280	3.371	0.331	6.320
	– 1.433	0.000	6.420	0.308	0.000	8.820
	– 1.186	0.332	6.420	0.761	0.218	8.820
60	– 0.893	0.570	6.420	1.222	0.389	8.820
%	– 0.552	0.715	6.420	1.699	0.470	8.820
	– 0.176	0.790	6.420	2.191	0.462	8.820
	0.217	0.832	6.420	2.691	0.410	8.820
	– 0.650	0.000	8.560	0.396	0.000	11.320
	– 0.541	0.172	8.560	0.651	0.144	11.320
80	– 0.414	0.318	8.560	0.914	0.261	11.320
%	– 0.255	0.419	8.560	1.190	0.330	11.320
	– 0.073	0.486	8.560	1.476	0.362	11.320
	0.122	0.535	8.560	1.768	0.374	11.320
	0.132	0.000	10.700	0.483	0.000	13.820
	0.144	0.016	10.700	0.511	0.012	13.820
100	0.159	0.030	10.700	0.538	0.023	13.820
%	0.173	0.044	10.700	0.567	0.033	13.820
	0.189	0.056	10.700	0.595	0.042	13.820
	0.207	0.066	10.700	0.624	0.051	13.820

(2) 96080248

AWA[deg]	TWIST[deg]	DRAFT[%]	AWS[m/s]	HEEL[deg]	VB [kt]
37.9	14.5	7.2	7.5	19.6	6.0
C_L	C_D	C_X	C_Y	x_{CE} [m]	z_{CE} [m]
1.58	0.45	0.62	1.52	0.34	4.17

% of heit	130%Jib x	130%Jib y	130%Jib z	Mainsail x	Mainsail y	Mainsail z
	– 3.780	0.000	0.000	0.046	0.000	1.320
	– 2.812	0.136	0.000	0.934	0.015	1.320
0	– 1.843	0.272	0.000	1.822	0.031	1.320
%	– 0.875	0.408	0.000	2.710	0.046	1.320
	0.094	0.544	0.000	3.597	0.062	1.320
	1.062	0.681	0.000	4.485	0.077	1.320
	– 2.998	0.000	2.140	0.133	0.000	3.820
	– 2.314	0.461	2.140	0.891	0.150	3.820
20	– 1.597	0.750	2.140	1.651	0.267	3.820
%	– 0.841	0.840	2.140	2.414	0.331	3.820
	– 0.062	0.810	2.140	3.182	0.333	3.820
	0.728	0.724	2.140	3.954	0.262	3.820
	– 2.215	0.000	4.280	0.221	0.000	6.320
	– 1.769	0.437	4.280	0.829	0.239	6.320
40	– 1.274	0.729	4.280	1.445	0.423	6.320
%	– 0.726	0.863	4.280	2.074	0.520	6.320
	– 0.145	0.899	4.280	2.717	0.511	6.320
	0.450	0.892	4.280	3.368	0.442	6.320
	– 1.433	0.000	6.420	0.308	0.000	8.820
	– 1.218	0.362	6.420	0.757	0.230	8.820
60	– 0.940	0.615	6.420	1.218	0.397	8.820
%	– 0.601	0.763	6.420	1.697	0.482	8.820
	– 0.230	0.854	6.420	2.187	0.504	8.820
	0.157	0.918	6.420	2.687	0.481	8.820
	– 0.650	0.000	8.560	0.396	0.000	11.320
	– 0.565	0.191	8.560	0.656	0.128	11.320
80	– 0.445	0.339	8.560	0.921	0.241	11.320
%	– 0.289	0.444	8.560	1.193	0.327	11.320
	– 0.113	0.527	8.560	1.478	0.368	11.320
	0.071	0.597	8.560	1.771	0.377	11.320
	0.132	0.000	10.700	0.483	0.000	13.820
	0.142	0.018	10.700	0.511	0.011	13.820
100	0.154	0.034	10.700	0.539	0.022	13.820
%	0.167	0.049	10.700	0.567	0.032	13.820
	0.181	0.064	10.700	0.596	0.041	13.820
	0.196	0.077	10.700	0.625	0.049	13.820

using the CCD cameras, but it was difficult to maintain a constant value of AWA for this length of time. So the aerodynamic data over a 30- to 60-s period was used. The boat was steered carefully during this time. However, the measured data contained some variation due to wind fluctuation and wave reflection on the hull.

Figure 6 shows an example of the measured data in the time domain for the AWA, AWS, heel angle and aerodynamic coefficients for 30 s recorded simultaneously at a sample rate of 10 Hz. In the figure, the averaged value of AWA over 5-s intervals and the aerodynamic coefficients are shown. Small fluctuations in the time history of the aerodynamic coefficients were caused by wave reflection on the hull, and these fluctuations can be eliminated by averaging the data in the time domain. Larger variations of the data are caused by deviations in the AWA, which were induced by fluctuations of the true wind angle and insufficient steering compensation. This example indicates the case for a relatively large deviation in AWA in order to show the correlation between the time histories of the AWA and each aerodynamic coefficient. In this case, when the data were averaged over 5-s intervals, the range of variation of C_X and C_Y was $\pm 7\%$, whereas the variation in AWA was $\pm 10\%$. Moreover, there was not much apparent time lag between changes in AWA and the changes in the coefficients. Therefore, it can be seen that

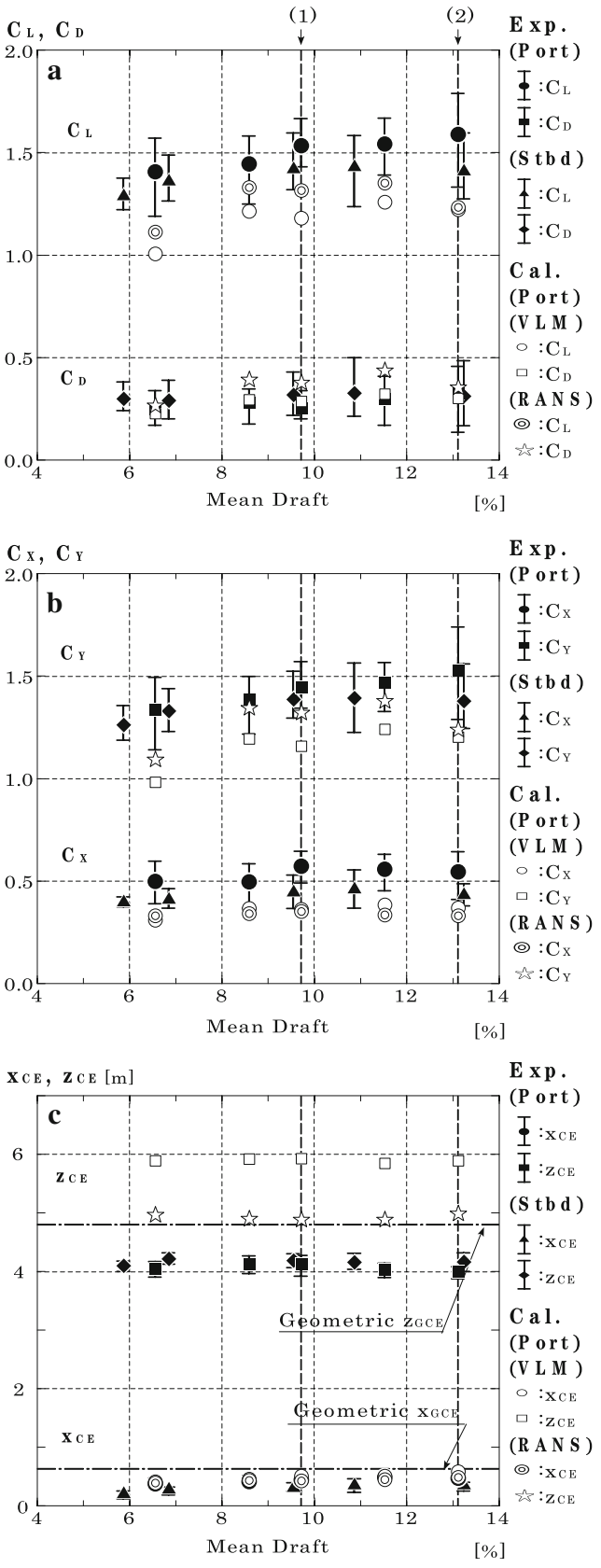

Fig. 11 Performance variation as a function of mainsail mean draft for mainsail and 130% jib. **a** C_L, C_D; **b** C_X, C_Y; **c** x_{CE}, z_{CE}

the correlations of the averaged values of AWA and each aerodynamic coefficient are very good.

However, it was difficult to keep the variation in AWA sufficiently small during the whole of a 90-s period. Therefore, the steady state values for the aerodynamic coefficients were obtained by averaging the data over a 30- to 60-s period in which the AWA was closer to the target value than it was during the whole 90-s period. For these tests, if the range of deviation of AWA exceeded ±5°, the results were discarded. All of the measured coefficients were plotted with error bars indicating the range of deviation over the averaging period.

3.5 Variation in wind velocity as a function of height over the testing area

Figure 7 shows the wind velocity as a function of height above the sea surface in this area. These wind velocities were measured using two anemometers set on the *Fujin* without sails. The solid circles indicate the data measured at the mast top (16.6 m above the sea surface) and bow unit (6.5 m). The open circles indicate the data measured by anemometers attached to the No. 1 spreader (10.0 m) and the No. 3 spreader (4.5 m). Two circles connected by a solid line or a dotted line show data measured simultaneously over a 30-s period using two anemometers. However, the data for the solid and the open circles were not measured at the same time. Therefore, the slope of the solid or dotted lines indicates the wind gradient at each height, respectively. In the figure, wind gradient curves indicating power–law profiles are also shown. The solid curves show a 1/10 power curve and the dotted curves a 1/7 power curve. It can be seen that the measured wind gradient in this area is not as large as either of these power–law profiles. Consequently, the wind gradient was not taken into account in the numerical calculations. This meant that the wind angle and speed at the inlet to the calculation field were assumed to be independent of height. The numerical calculations were performed using the wind angle and speed which were measured at the bow unit, i.e., at the height of the GCE of the sail plan.

4 Numerical calculation method

4.1 Vortex lattice method

As a potential flow calculation, a vortex lattice method was employed to compare with the results of a RANS-based CFD calculation. The sail surface was divided into rectangular panels, and a horseshoe bound vortex was placed

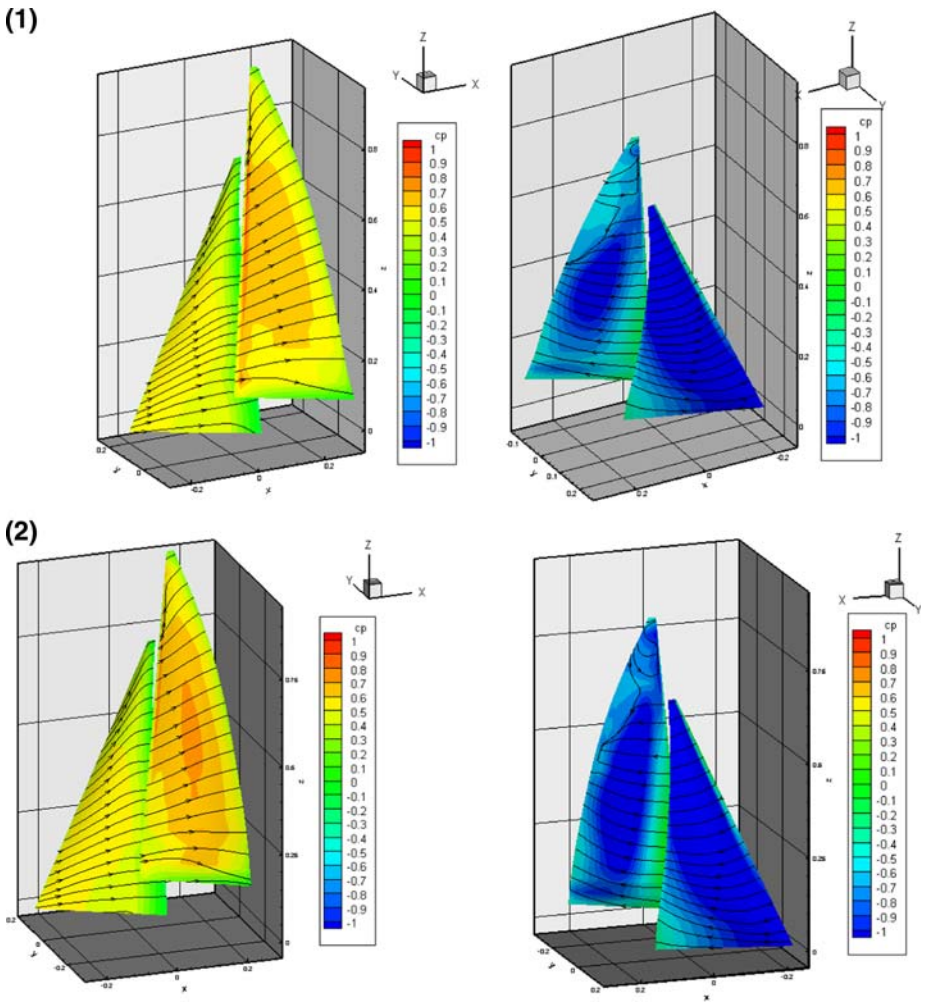

Fig. 12 (1) Surface pressure and streamlines obtained by RANS-based CFD for experimental ID 96092336 (mean draft = 9.7%). (2) Surface pressure and streamlines obtained by RANS-based CFD at experimental ID 9609233A (mean draft = 13.1%)

on each panel at a distance of one-quarter panel length from the fore end of the panel with free wake vortices proceeding downstream from the trailing edge of the sail. The shapes and positions of the wake vortices were determined so that they were parallel to the local velocity field induced by the total vortex system.

A step-by-step procedure developed by Fukasawa [7] was used to determine the strength of the bound vortices and the location of wake vortices; this procedure was iterated until the calculated lift and drag forces converged. The strengths of the bound vortices were determined so as to satisfy the boundary condition on the sail at the control points, which were placed on each panel at a distance of one-quarter panel length from the aft end of the panel. Wake vortices were shed from the trailing edge of the sail at each time step. Maintaining the vortex strength, the shed vortex filament moved downstream at the local field velocity in the direction of the field velocity vector, which was updated at every time step. Once all the vortex strengths were determined, the lift, induced drag, and moments acting on the sail were calculated. The detailed procedure was described in previous articles [2, 6].

Since the vortex lattice methods do not predict viscous drag, the viscous drag acting on the sails and rigging was calculated empirically using a drag coefficient, C_{Dp}. The value of C_{Dp} was obtained from the measured data in the previous articles and formulated for the upwind condition as follows:

$$C_{\mathrm{Dp}} = 0.0026\gamma_{\mathrm{A}} + 0.005 \tag{2}$$

where γ_{A} is the apparent wind angle in degrees.

As noted above, the shape of the sail was reanalyzed compared to the results in the previous articles, and hence all the calculations were repeated for the new shapes. In the calculations, each sail plane was divided into 200 panels; that is, 20 panels in the vertical direction and 10 panels in the horizontal direction. The mirror image of the sail was taken into account about the sea surface.

Table 4 Sail shapes, measured experimental data and three-dimensional coordinates of the sails for the cases of (1) 96092335 and (2) 96080248

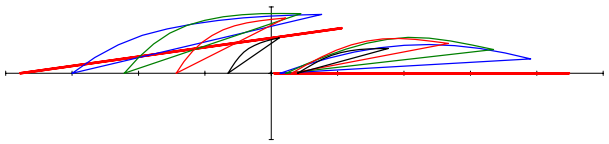

(1) 96092336

AWA[deg]	TWIST[deg]	DRAFT[%]	AWS[m/s]	HEEL[deg]	VB [kt]
30.9	15.5	9.7	7.5	19.8	5.5
C_L	C_D	C_X	C_Y	x_{CE} [m]	z_{CE} [m]
1.53	0.25	0.57	1.45	0.44	4.12

% of heit	130%Jib x	130%Jib y	130%Jib z	Mainsail x	Mainsail y	Mainsail z
	– 3.780	0.000	0.000	0.046	0.000	1.320
	– 2.812	0.136	0.000	0.934	0.000	1.320
0	– 1.843	0.272	0.000	1.822	0.000	1.320
%	– 0.875	0.408	0.000	2.710	0.000	1.320
	0.094	0.544	0.000	3.598	0.000	1.320
	1.062	0.681	0.000	4.486	0.000	1.320
	– 2.998	0.000	2.140	0.133	0.000	3.820
	– 2.305	0.429	2.140	0.878	0.232	3.820
20	– 1.568	0.667	2.140	1.626	0.385	3.820
%	– 0.805	0.795	2.140	2.381	0.433	3.820
	– 0.027	0.861	2.140	3.141	0.373	3.820
	0.760	0.886	2.140	3.908	0.216	3.820
	– 2.215	0.000	4.280	0.221	0.000	6.320
	– 1.771	0.442	4.280	0.825	0.259	6.320
40	– 1.272	0.719	4.280	1.437	0.451	6.320
%	– 0.723	0.850	4.280	2.060	0.541	6.320
	– 0.145	0.898	4.280	2.700	0.488	6.320
	0.448	0.898	4.280	3.348	0.356	6.320
	– 1.433	0.000	6.420	0.308	0.000	8.820
	– 1.186	0.332	6.420	0.751	0.243	8.820
60	– 0.893	0.570	6.420	1.205	0.427	8.820
%	– 0.552	0.715	6.420	1.677	0.518	8.820
	– 0.176	0.790	6.420	2.168	0.509	8.820
	0.217	0.832	6.420	2.669	0.449	8.820
	– 0.650	0.000	8.560	0.396	0.000	11.320
	– 0.541	0.172	8.560	0.649	0.149	11.320
80	– 0.414	0.318	8.560	0.910	0.270	11.320
%	– 0.255	0.419	8.560	1.185	0.340	11.320
	– 0.073	0.486	8.560	1.471	0.368	11.320
	0.122	0.535	8.560	1.764	0.373	11.320
	0.132	0.000	10.700	0.483	0.000	13.820
	0.144	0.016	10.700	0.511	0.012	13.820
100	0.159	0.030	10.700	0.538	0.023	13.820
%	0.173	0.044	10.700	0.567	0.033	13.820
	0.189	0.056	10.700	0.595	0.042	13.820
	0.207	0.066	10.700	0.624	0.051	13.820

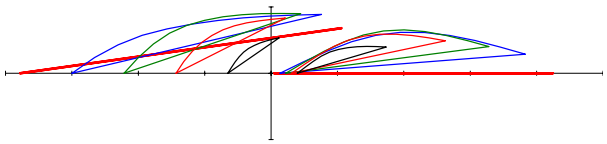

(2) 9609233A

AWA[deg]	TWIST[deg]	DRAFT[%]	AWS[m/s]	HEEL[deg]	VB [kt]
30.9	16.6	13.1	7.0	16.9	5.4
C_L	C_D	C_X	C_Y	x_{CE} [m]	z_{CE} [m]
1.59	0.33	0.54	1.53	0.47	3.99

% of heit	130%Jib x	130%Jib y	130%Jib z	Mainsail x	Mainsail y	Mainsail z
	– 3.780	0.000	0.000	0.046	0.000	1.320
	– 2.812	0.136	0.000	0.886	0.000	1.320
0	– 1.843	0.272	0.000	1.726	0.000	1.320
%	– 0.875	0.408	0.000	2.566	0.000	1.320
	0.094	0.544	0.000	3.406	0.000	1.320
	1.062	0.681	0.000	4.246	0.000	1.320
	– 2.998	0.000	2.140	0.133	0.000	3.820
	– 2.305	0.429	2.140	0.851	0.336	3.820
20	– 1.568	0.667	2.140	1.577	0.572	3.820
%	– 0.805	0.795	2.140	2.318	0.614	3.820
	– 0.027	0.861	2.140	3.071	0.493	3.820
	0.760	0.886	2.140	3.831	0.286	3.820
	– 2.215	0.000	4.280	0.221	0.000	6.320
	– 1.771	0.442	4.280	0.800	0.331	6.320
40	– 1.272	0.719	4.280	1.391	0.576	6.320
%	– 0.723	0.850	4.280	2.004	0.653	6.320
	– 0.145	0.898	4.280	2.638	0.570	6.320
	0.448	0.898	4.280	3.283	0.403	6.320
	– 1.433	0.000	6.420	0.308	0.000	8.820
	– 1.186	0.332	6.420	0.733	0.284	8.820
60	– 0.893	0.570	6.420	1.171	0.501	8.820
%	– 0.552	0.715	6.420	1.637	0.589	8.820
	– 0.176	0.790	6.420	2.126	0.568	8.820
	0.217	0.832	6.420	2.628	0.490	8.820
	– 0.650	0.000	8.560	0.396	0.000	11.320
	– 0.541	0.172	8.560	0.634	0.180	11.320
80	– 0.414	0.318	8.560	0.885	0.319	11.320
%	– 0.255	0.419	8.560	1.156	0.386	11.320
	– 0.073	0.486	8.560	1.442	0.404	11.320
	0.122	0.535	8.560	1.736	0.395	11.320
	0.132	0.000	10.700	0.483	0.000	13.820
	0.144	0.016	10.700	0.511	0.012	13.820
100	0.159	0.030	10.700	0.538	0.024	13.820
%	0.173	0.044	10.700	0.566	0.035	13.820
	0.189	0.056	10.700	0.595	0.044	13.820
	0.207	0.066	10.700	0.623	0.054	13.820

4.2 Multiblock RANS-based CFD method

The RANS-based CFD method used in the present study was FLOWPACK version 2005. The code was developed by Tahara specifically for CFD education and research and for design applications for ship hydrodynamics, aerodynamics, and fluid engineering. As part of the developments for application to design problems, a complete multiblock domain decomposition feature was included. At present, FLOWPACK has a good interface with the authors' in-house automatic grid generator as well as with commercial grid generation software.

The numerical method of FLOWPACK solves the unsteady Reynolds-averaged Navier–Stokes and continuity equations for mean velocity and pressure. Either a zero or a two-equation turbulence model can be used for turbulent flow calculation, and in the present study, the former was used, as described below.

The equations were transformed from Cartesian coordinates in the physical domain to numerically generated, boundary-fitted, nonorthogonal, curvilinear coordinates in the computational domain. A partial transformation was used, i.e., the coordinates were transformed but not the velocity components. The equations were solved using a

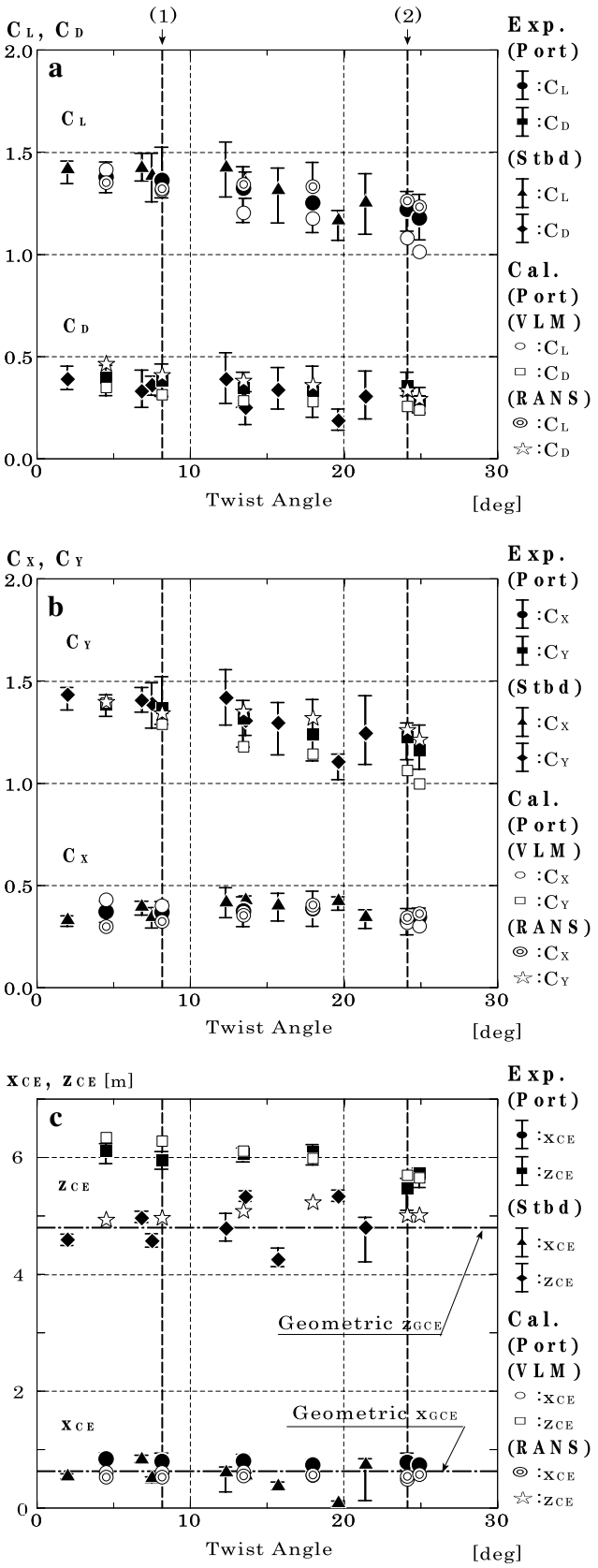

Fig. 13 Performance variation as a function of mainsail twist angle for mainsail and 130% jib. **a** C_L, C_D; **b** C_X, C_Y; **c** x_{CE}, z_{CE}

regular grid, finite-analytic spatial and first-order backward difference temporal discretization, and a pressure implicit with splitting of operators (PISO)-type pressure algorithm.

The present RANS code was applied to predict the flow field around the sail configurations in the series obtained from the measurements. Figure 8 shows an overview of the computational grid for the present upwind sail system. An automatic gridding scheme developed by the authors was used. The total number of grids was around half a million and the number of multiblocks was 48. Input data for the present automatic gridding scheme were the measured sail geometry, the AWA, and the heel angle. In the computations, the Reynolds number, Re, was 5×10^6 (based on the apparent wind speed and mast height), which corresponded to the full-scale condition.

The aforementioned grid size and turbulence model were determined based on the authors' previous work on downwind sail systems [15]. For the present numerical method, the focus was more on an initial validation of the method to investigate its capabilities and limitations through many case studies; hence, a moderate grid size, along with a relatively simple algebraic turbulence model, i.e., the Baldwin–Lomax model, was used to give a high computational efficiency. We have been encouraged by the recent trends in rapidly increasing computer power, and we will continue this work further to investigate the capabilities of the present CFD approach by using a higher-order turbulence model together with a finer computational grid (of the order of several millions), and the results will be reported in the near future.

In the present study, the mast and rigging were not considered for the series calculations, and the bottom surface of the computational grid was taken as the deck plane of the boat. In a separate section, the influences of the mast on flow and forces are discussed.

5 Comparison between experimental and calculated results

In this section, the experimental results and the calculated results for the following cases will be compared:

1. Mainsail with 130% jib:
   a. Variation with apparent wind angle
   b. Variation with mainsail mean draft
   c. Variation with mainsail twist angle
2. Mainsail with 75% jib:
   a. Variation with apparent wind angle
3. Mainsail alone:
   a. Variation with mainsail twist angle.

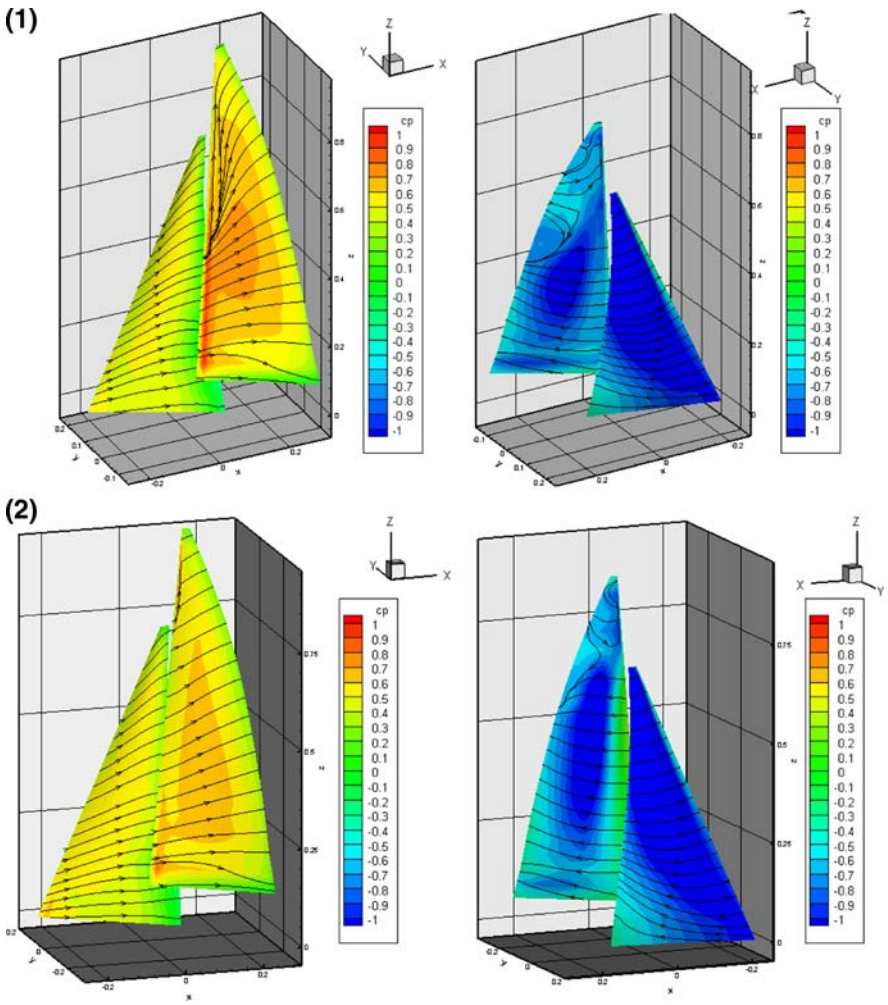

Fig. 14 (1) Surface pressure and streamlines obtained by RANS-based CFD at experimental ID 97072213 (twist angle = 8.2°). (2) Surface pressure and streamlines obtained by RANS-based CFD at experimental ID 97072218 (twist angle = 24.1°)

For each series, first the sail coefficients C_L, C_D, C_X, and C_Y and the coordinates of x_{CE} and z_{CE} are given. Then, the sail surface pressure and streamlines calculated using the RANS-based CFD procedure are presented for two typical cases in each series. Finally, the shapes and three-dimensional coordinates of the sails are tabulated for each case corresponding to those where the RANS-based CFD results are given.

5.1 Mainsail with 130% Jib

5.1.1 Variation with apparent wind angle

Figure 9 shows the performance variation for the mainsail and 130% jib configuration as a function of AWA. In the figure, the solid symbols indicate the experimental results and the open symbols indicate the calculated results using the VLM and the RANS-based CFD. For the experimental results, data from both the starboard and port tack are shown. All measured coefficients are plotted with error bars indicating the range of deviation over the averaging period. There were some discrepancies between the data from each tack. During the experiments, efforts were made to remove this asymmetrical performance; however, the boat speed actually differed on each tack. It can be concluded that there was a slight asymmetry in the combination of the hull, keel, rudder, and dynamometer frame.

The experimental data in this figure coincide those in Fig. 17 in a previous article [6]. However, some data points from the previous article were eliminated due to the lack of sail shape information or bad sail trimming. In order to describe the error bars on the data points, all of recorded time domain data were reviewed and the range of deviation over the averaging period was determined. The numerical calculations were performed using the measured shape data. In order to avoid confusion when interpreting the figure, the calculated results are indicated only for the port tack. Therefore, the calculated and experimental points for the port tack correspond.

In this figure, AWA ranges from 20.3° to 37.9° for the port tack. The former is the closest angle to the wind that was achieved, and the latter is typical of a close reaching

Table 5 Sail shapes, measured experimental data and three-dimensional coordinates of the sails for the cases of (1) 97072213 and (2) 97072218

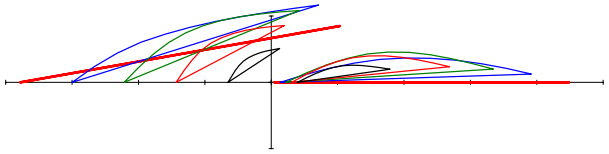

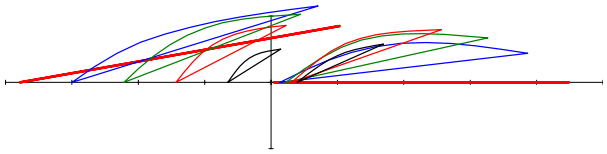

(1) 97072213

AWA[deg]	TWIST[deg]	DRAFT[%]	AWS[m/s]	HEEL[deg]	VB [kt]
30.7	8.2	10.5	7.3	16.8	5.1
C_L	C_D	C_X	C_Y	x_{CE} [m]	z_{CE} [m]
1.36	0.38	0.37	1.37	0.79	5.96

% of heit	130%Jib			Mainsail		
	x	y	z	x	y	z
	– 3.780	0.000	0.000	0.046	0.000	1.320
	– 2.817	0.170	0.000	0.934	0.000	1.320
0	– 1.854	0.340	0.000	1.822	0.000	1.320
%	– 0.891	0.509	0.000	2.710	0.000	1.320
	0.073	0.679	0.000	3.598	0.000	1.320
	1.036	0.849	0.000	4.486	0.000	1.320
	– 2.998	0.000	2.140	0.133	0.000	3.820
	– 2.320	0.440	2.140	0.884	0.214	3.820
20	– 1.595	0.727	2.140	1.638	0.345	3.820
%	– 0.839	0.917	2.140	2.395	0.362	3.820
	– 0.067	1.055	2.140	3.156	0.283	3.820
	0.714	1.165	2.140	3.919	0.125	3.820
	– 2.215	0.000	4.280	0.221	0.000	6.320
	– 1.774	0.427	4.280	0.832	0.263	6.320
40	– 1.289	0.746	4.280	1.449	0.427	6.320
%	– 0.750	0.933	4.280	2.076	0.452	6.320
	– 0.174	1.031	4.280	2.710	0.358	6.320
	0.421	1.082	4.280	3.348	0.199	6.320
	– 1.433	0.000	6.420	0.308	0.000	8.820
	– 1.193	0.336	6.420	0.766	0.231	8.820
60	– 0.911	0.590	6.420	1.232	0.372	8.820
%	– 0.573	0.737	6.420	1.710	0.399	8.820
	– 0.199	0.816	6.420	2.196	0.340	8.820
	0.196	0.855	6.420	2.687	0.235	8.820
	– 0.650	0.000	8.560	0.396	0.000	11.320
	– 0.543	0.176	8.560	0.662	0.130	11.320
80	– 0.416	0.322	8.560	0.932	0.224	11.320
%	– 0.255	0.414	8.560	1.212	0.259	11.320
	– 0.070	0.472	8.560	1.499	0.241	11.320
	0.128	0.510	8.560	1.789	0.197	11.320
	0.132	0.000	10.700	0.483	0.000	13.820
	0.145	0.016	10.700	0.512	0.007	13.820
100	0.161	0.028	10.700	0.541	0.014	13.820
%	0.177	0.041	10.700	0.571	0.019	13.820
	0.193	0.052	10.700	0.601	0.023	13.820
	0.212	0.060	10.700	0.630	0.027	13.820

(2) 97072218

AWA[deg]	TWIST[deg]	DRAFT[%]	AWS[m/s]	HEEL[deg]	VB [kt]
31.1	24.1	10.6	7.2	12.3	5.1
C_L	C_D	C_X	C_Y	x_{CE} [m]	z_{CE} [m]
1.22	0.36	0.33	1.23	0.78	5.47

% of heit	130%Jib			Mainsail		
	x	y	z	x	y	z
	– 3.780	0.000	0.000	0.046	0.000	1.320
	– 2.817	0.170	0.000	0.934	0.000	1.320
0	– 1.854	0.340	0.000	1.822	0.000	1.320
%	– 0.891	0.509	0.000	2.710	0.000	1.320
	0.073	0.679	0.000	3.598	0.000	1.320
	1.036	0.849	0.000	4.486	0.000	1.320
	– 2.998	0.000	2.140	0.133	0.000	3.820
	– 2.321	0.439	2.140	0.852	0.328	3.820
20	– 1.598	0.728	2.140	1.584	0.539	3.820
%	– 0.844	0.914	2.140	2.334	0.601	3.820
	– 0.073	1.048	2.140	3.097	0.548	3.820
	0.708	1.151	2.140	3.866	0.437	3.820
	– 2.215	0.000	4.280	0.221	0.000	6.320
	– 1.760	0.403	4.280	0.777	0.378	6.320
40	– 1.266	0.707	4.280	1.358	0.638	6.320
%	– 0.729	0.898	4.280	1.977	0.730	6.320
	– 0.151	0.985	4.280	2.617	0.721	6.320
	0.444	1.025	4.280	3.268	0.669	6.320
	– 1.433	0.000	6.420	0.308	0.000	8.820
	– 1.173	0.313	6.420	0.701	0.328	8.820
60	– 0.883	0.565	6.420	1.119	0.582	8.820
%	– 0.544	0.724	6.420	1.580	0.716	8.820
	– 0.168	0.811	6.420	2.068	0.771	8.820
	0.229	0.858	6.420	2.568	0.794	8.820
	– 0.650	0.000	8.560	0.396	0.000	11.320
	– 0.533	0.166	8.560	0.627	0.179	11.320
80	– 0.401	0.310	8.560	0.868	0.335	11.320
%	– 0.243	0.411	8.560	1.127	0.453	11.320
	– 0.056	0.467	8.560	1.406	0.525	11.320
	0.146	0.500	8.560	1.694	0.576	11.320
	0.132	0.000	10.700	0.483	0.000	13.820
	0.145	0.016	10.700	0.509	0.015	13.820
100	0.161	0.028	10.700	0.535	0.031	13.820
%	0.177	0.040	10.700	0.561	0.045	13.820
	0.193	0.052	10.700	0.588	0.057	13.820
	0.212	0.060	10.700	0.615	0.070	13.820

condition, in which the sail is trimmed in the power down mode. There is some scatter in the experimental data because they are made up from measurements taken with the sails trimmed in slightly different ways. The experimental value of C_L in Fig. 9a varies with AWA from 0.91 to 1.58. For the close reaching condition, the sails were not well trimmed to satisfy the power down mode. A sample of the measured sail sections in this condition is shown in the figure associated with Table 3(2): it can be seen that both the mainsail and the jib are not eased sufficiently to correspond to the large AWA. This is the reason for the decrement in the measured lift curve slope of C_L for AWA angles greater then about 35°.

The calculated results for C_L using the VLM show good agreement with the experiments at AWA angles less than about 35°. Above about 35°, the calculated results are lower than the measured ones. This shows that the calculated results strongly indicate the effect of incorrect sail trimming. The results for C_L using the RANS-based CFD show the same trends as the experimental results, but have slight higher values than those from the experiments for AWAs between 20° and 30° and lower values for AWAs

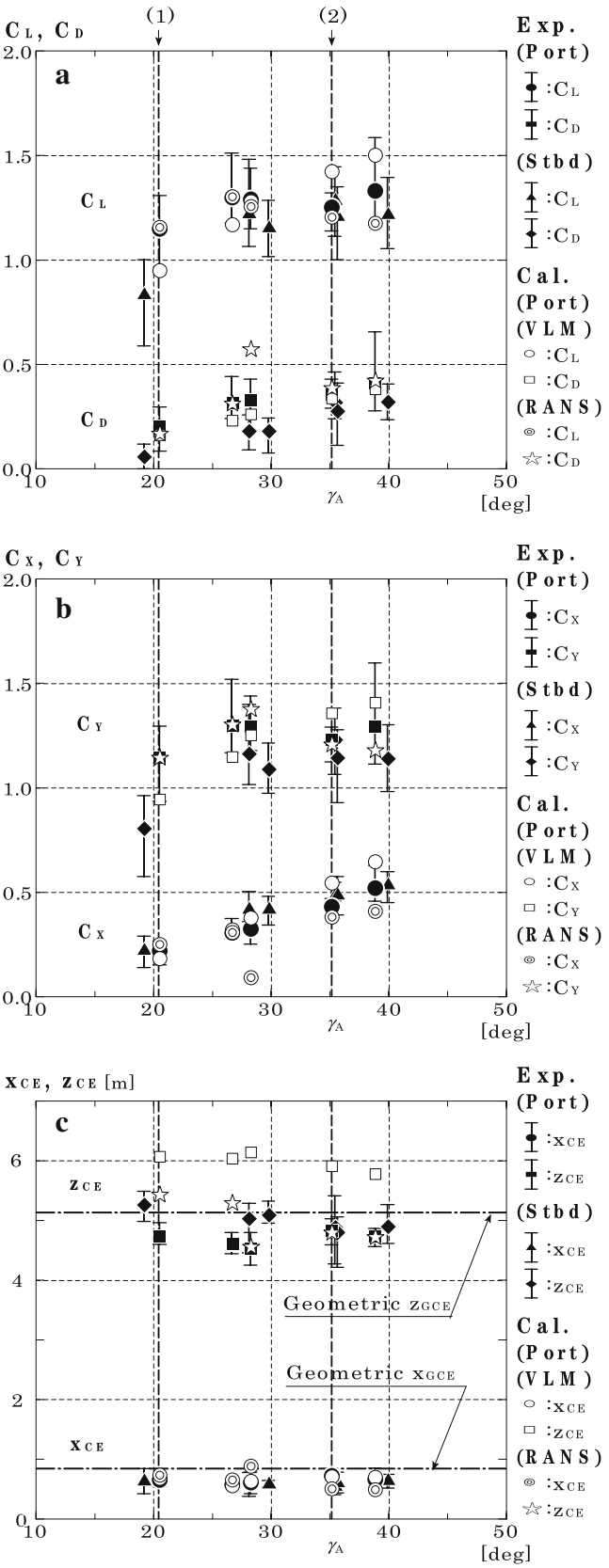

Fig. 15 Performance variation as a function of AWA for mainsail and 75% jib. **a** C_L, C_D; **b** C_X, C_Y; **c** x_{CE}, z_{CE}

greater than 30°. In particular, the decrease in C_L for AWA values greater than 30° is considerably large. This will be discussed later with the calculated sail surface pressure and streamlines. The calculated results for C_D slightly over-predict those from the experiments.

Figure 9c shows the coordinates of the center of effort of the sails. The x and z coordinates of the geometric center of effort (x_{GCE} and z_{GCE}) are 0.63 m aft and 4.80 m above the origin, which are indicated by alternate long and short dashed lines in the figure. It is seen that both the experimental and the calculated coordinates of x_{CE} are close to x_{GCE} and move slightly forward with increasing AWA. Unfortunately, there is a wide scatter in the experimental values of z_{CE}. This is thought to be because the measured *Ks* moment contains a large component from the mass of the dynamometer frame and rigging (659 kg). This moment was subtracted from the measurement, taking into account the measured heel angle. If there is a slight error in the position of center of gravity of the dynamometer frame, or in the measured heel angle, the error in the calculated moment will be large. However, although there is some scatter in the measured data, it can be seen that z_{CE} decreases as AWA increases. The trends in the movement of both x_{CE} and z_{CE} as functions of AWA might be caused by the decrement of force acting on the aft and upper parts of the sails due to the loosening of the main and jib sheets with increasing AWA. The calculated results for z_{CE} obtained using the RANS-based CFD show the same trend as for the experiments. In contrast, the calculated results using VLM are considerably higher than the experimental results. This might be caused by overestimation of the force acting on the upper portion of the mainsail. In this area, since the jib is not overlapping, flow separation may occur easily. However, the VLM does not take flow separation into account.

Figure 10(1) and (2) shows the calculated results of the sail surface pressure and streamlines using RANS-based CFD. Figure 10(1) shows the results for experimental ID 96092335 (AWA = 30.7°) and Fig. 10(2) shows the results for ID 96080248 (AWA = 37.9°). These data correspond to the plotted points on the vertical dotted lines (1) and (2) in Fig. 9. In Fig. 10, the left and right diagrams correspond to the port and starboard sides, i.e., the pressure and suction sides, respectively. In Fig. 10(1), although slight flow separation on the suction side of the mainsail is seen, the streamlines of both sides run smoothly. On the other hand, in Fig. 10(2), considerable flow separation occurs, in particular, on the suction side of jib. This is the main reason for the reduction of C_L in the RANS-based CFD calculation at (2) in Fig. 9a. This will be discussed further in the following chapter.

The shapes and three-dimensional coordinates of the sails are given in Table 3. These also correspond to the

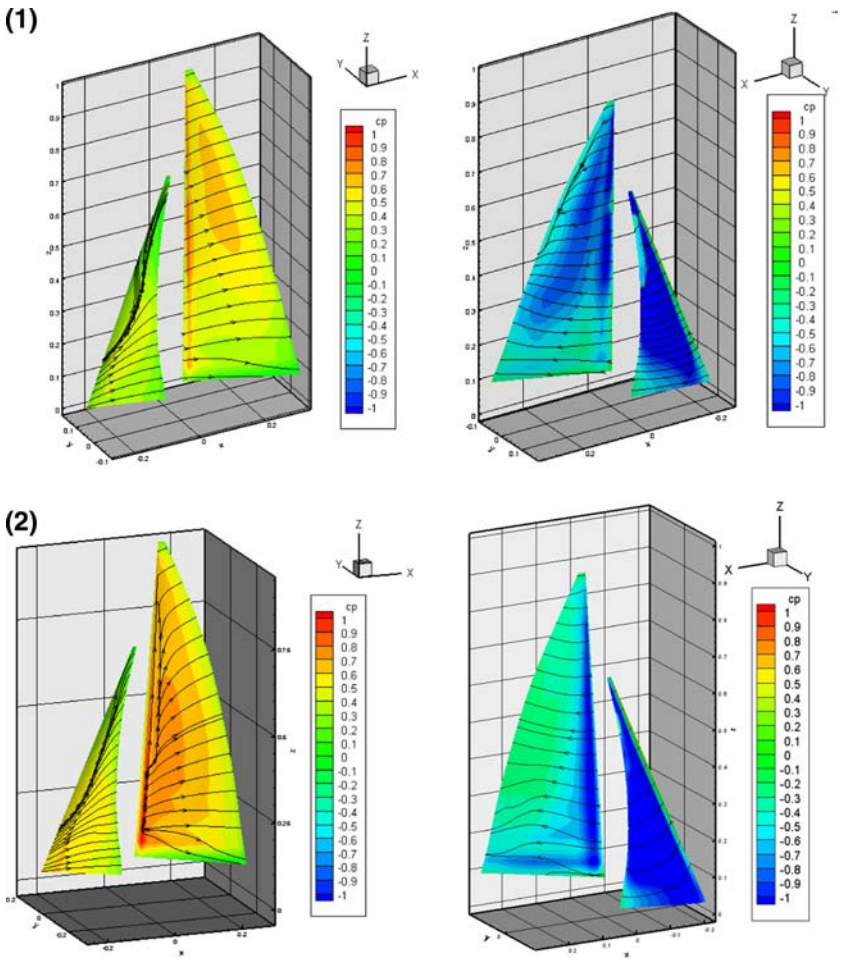

Fig. 16 (1) Surface pressure and streamlines obtained by RANS-based CFD at experimental ID 98110105 (AWA = 20.5°). (2) Surface pressure and streamlines obtained by RANS-based CFD at experimental ID 9811032A (AWA = 35.2°)

calculated results shown in Fig. 10. The figures described above the tables show the sail section profiles at 0, 20, 40, 60, and 80% of the sail height. The dimensions of these three-dimensional coordinates are given in the tables, including 100% height section data. The coordinate system is given in Fig. 1. The positive direction of the x coordinate is aft. The four lines at the top of the tables show the measured values for the wind and sail trim conditions, the boat attitude, and the sail performance coefficients.

5.1.2 Variation with mainsail mean draft

Figure 11 shows the performance variation for the mainsail and 130% jib configuration as a function of mainsail mean draft. The notations for all figures in this section are the same as those in the former section.

The mainsail draft was changed by varying the backstay and check-stay tensions and the position of the mainsail outhaul. The twist of the mainsail was controlled to keep the exit angle of the top batten parallel with the boom angle by varying the main sheet tension. The experiment was performed for an average value of AWA of 30° ± 2° with the twist angle at around 16°. The jib shape was fixed. The mean draft is defined as the average of the maximum draft of four evenly spaced sections of the mainsail from 20 to 80% height.

In the figure, the mean draft ranges from 6.6 to 13.1% for the port tack. Varying the mean draft by 6.5%, the value of C_X in Fig. 11b changes from 0.50 to 0.57 (14%), and the value of C_Y from 1.34 to 1.53 (14%). It can be seen that the maximum C_X (i.e. thrust) occurs at a mean draft of around 10–12%. Although the calculated results for C_X and C_Y have slightly lower values than the measured results, the trend as a function of mean draft is correct.

Figure 12 shows the calculated results using RANS-based CFD corresponding to experimental ID 96092336 (mean draft = 9.7%) and to ID 9609233A (mean draft = 13.1%). It can be seen that the high pressure area on the pressure side of the mainsail with the higher mean draft, shown in Fig. 12(2), is further aft than that in Fig. 12(1) where the mean draft is smaller. This results in a lower thrust force on the mainsail and hence a lower value of C_X at (2) in Fig. 11b. Table 4 shows the shapes and three-dimensional coordinates of the sails for the cases 1 and 2, which correspond to the calculated results shown in Fig. 12.

Table 6 Sail shapes, measured experimental data and three-dimensional coordinates of the sails for the cases of (1) 98110105 and (2) 9811032A

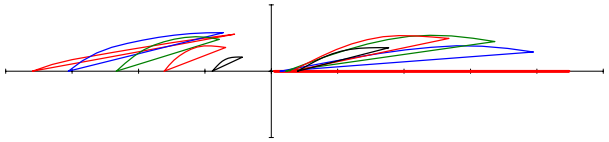

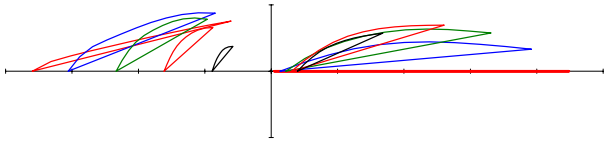

(1) 98110105

AWA[deg]	TWIST[deg]	DRAFT[%]	AWS[m/s]	HEEL[deg]	VB [kt]
20.5	14.5	7.9	8.6	11.6	4.8
C_L	C_D	C_X	C_Y	x_{CE} [m]	z_{CE} [m]
1.15	0.20	0.22	1.15	0.65	4.73

% of heit	75%Jib x	75%Jib y	75%Jib z	Mainsail x	Mainsail y	Mainsail z
Jib	– 3.599	0.000	0.495	0.046	0.000	1.32
5%	– 3.001	0.173	0.495	0.934	0.000	1.32
	– 2.392	0.282	0.495	1.822	0.000	1.32
Main	– 1.780	0.384	0.495	2.710	0.000	1.32
0%	– 1.168	0.476	0.495	3.598	0.000	1.32
	– 0.553	0.557	0.495	4.486	0.000	1.32
	– 3.057	0.000	1.980	0.133	0.000	3.820
	– 2.630	0.274	1.980	0.890	0.142	3.820
20	– 2.170	0.418	1.980	1.648	0.271	3.820
%	– 1.697	0.511	1.980	2.409	0.361	3.820
	– 1.215	0.567	1.980	3.175	0.375	3.820
	– 0.723	0.581	1.980	3.949	0.289	3.820
	– 2.335	0.000	3.960	0.221	0.000	6.320
	– 2.065	0.228	3.960	0.831	0.223	6.320
40	– 1.776	0.391	3.960	1.447	0.409	6.320
%	– 1.464	0.481	3.960	2.073	0.524	6.320
	– 1.136	0.520	3.960	2.714	0.531	6.320
	– 0.783	0.479	3.960	3.368	0.448	6.320
	– 1.612	0.000	5.940	0.308	0.000	8.820
	– 1.464	0.167	5.940	0.755	0.226	8.820
60	– 1.298	0.287	5.940	1.211	0.411	8.820
%	– 1.115	0.365	5.940	1.683	0.519	8.820
	– 0.908	0.380	5.940	2.175	0.532	8.820
	– 0.687	0.358	5.940	2.677	0.495	8.820
	– 0.890	0.000	7.920	0.396	0.000	11.320
	– 0.816	0.080	7.920	0.652	0.143	11.320
80	– 0.738	0.150	7.920	0.914	0.261	11.320
%	– 0.648	0.196	7.920	1.189	0.330	11.320
	– 0.546	0.213	7.920	1.476	0.353	11.320
	– 0.435	0.212	7.920	1.769	0.353	11.320
	– 0.167	0.000	9.900	0.483	0.000	13.820
	– 0.152	0.014	9.900	0.511	0.010	13.820
100	– 0.135	0.025	9.900	0.540	0.020	13.820
%	– 0.118	0.036	9.900	0.568	0.029	13.820
	– 0.101	0.045	9.900	0.597	0.036	13.820
	– 0.081	0.052	9.900	0.626	0.044	13.820

(2) 9811032A

AWA[deg]	TWIST[deg]	DRAFT[%]	AWS[m/s]	HEEL[deg]	VB [kt]
35.2	24.4	9.5	7.6	9.6	5.9
C_L	C_D	C_X	C_Y	x_{CE} [m]	z_{CE} [m]
1.25	0.36	0.43	1.23	0.72	4.82

% of heit	75%Jib x	75%Jib y	75%Jib z	Mainsail x	Mainsail y	Mainsail z
Jib	– 3.599	0.000	0.495	0.046	0.000	1.32
5%	– 3.020	0.231	0.495	0.934	0.000	1.32
	– 2.420	0.377	0.495	1.822	0.000	1.32
Main	– 1.817	0.514	0.495	2.710	0.000	1.32
0%	– 1.212	0.641	0.495	3.598	0.000	1.32
	– 0.604	0.756	0.495	4.486	0.000	1.32
	– 3.057	0.000	1.980	0.133	0.000	3.820
	– 2.691	0.370	1.980	0.875	0.248	3.820
20	– 2.254	0.561	1.980	1.625	0.400	3.820
%	– 1.810	0.733	1.980	2.384	0.442	3.820
	– 1.345	0.853	1.980	3.151	0.406	3.820
	– 0.842	0.876	1.980	3.920	0.331	3.820
	– 2.335	0.000	3.960	0.221	0.000	6.320
	– 2.148	0.310	3.960	0.798	0.338	6.320
40	– 1.914	0.539	3.960	1.402	0.528	6.320
%	– 1.635	0.689	3.960	2.024	0.624	6.320
	– 1.327	0.787	3.960	2.663	0.627	6.320
	– 0.961	0.784	3.960	3.312	0.576	6.320
	– 1.612	0.000	5.940	0.308	0.000	8.820
	– 1.527	0.201	5.940	0.715	0.312	8.820
60	– 1.422	0.378	5.940	1.152	0.527	8.820
%	– 1.281	0.518	5.940	1.619	0.639	8.820
	– 1.107	0.619	5.940	2.107	0.685	8.820
	– 0.878	0.659	5.940	2.606	0.695	8.820
	– 0.890	0.000	7.920	0.396	0.000	11.320
	– 0.855	0.099	7.920	0.612	0.205	11.320
80	– 0.815	0.193	7.920	0.851	0.362	11.320
%	– 0.764	0.278	7.920	1.114	0.464	11.320
	– 0.694	0.347	7.920	1.393	0.529	11.320
	– 0.576	0.375	7.920	1.682	0.573	11.320
	– 0.167	0.000	9.900	0.483	0.000	13.820
	– 0.161	0.020	9.900	0.508	0.016	13.820
100	– 0.152	0.037	9.900	0.533	0.033	13.820
%	– 0.141	0.054	9.900	0.560	0.047	13.820
	– 0.131	0.071	9.900	0.586	0.061	13.820
	– 0.117	0.087	9.900	0.613	0.075	13.820

5.1.3 Variation with mainsail twist angle

Figure 13 shows the performance variation for the mainsail and 130% jib configuration as a function of mainsail twist angle. The mainsail twist was changed by varying the main sheet tension. The boom angle was kept parallel with the boat centerline by moving the main sheet traveler. The experiment was performed for an average value of AWA of 30° ± 2° and a mean draft of around 10%. The jib shape was fixed. The twist angle is defined as the angle between the boom line and section chord line at 80% height.

In the figure, the twist angle ranges from 4.5° to 24.9° for the port tack. Varying the twist angle by 20.4° resulted in the value of C_X in Fig. 13b changing from 0.33 to 0.39 (18%) and in the value of C_Y changing from 1.16 to 1.39 (20%). It can be seen that the maximum C_X (i.e., thrust) occurs at a twist angle of around 15°. The considerable decrease in C_Y with increasing twist angle is also worth noting. In this case, the calculated results for C_X and C_Y and C_L and C_D corresponded to the measured values very well.

Figure 14 shows the calculated results using RANS-based CFD. Figure 14(1) corresponds to experimental ID 97072213 (twist angle = 8.2°), and Fig. 14(2) corresponds to ID 97072218 (twist angle = 24.1°). It can be seen in Fig. 14(1) that the streamlines on the upper part of the

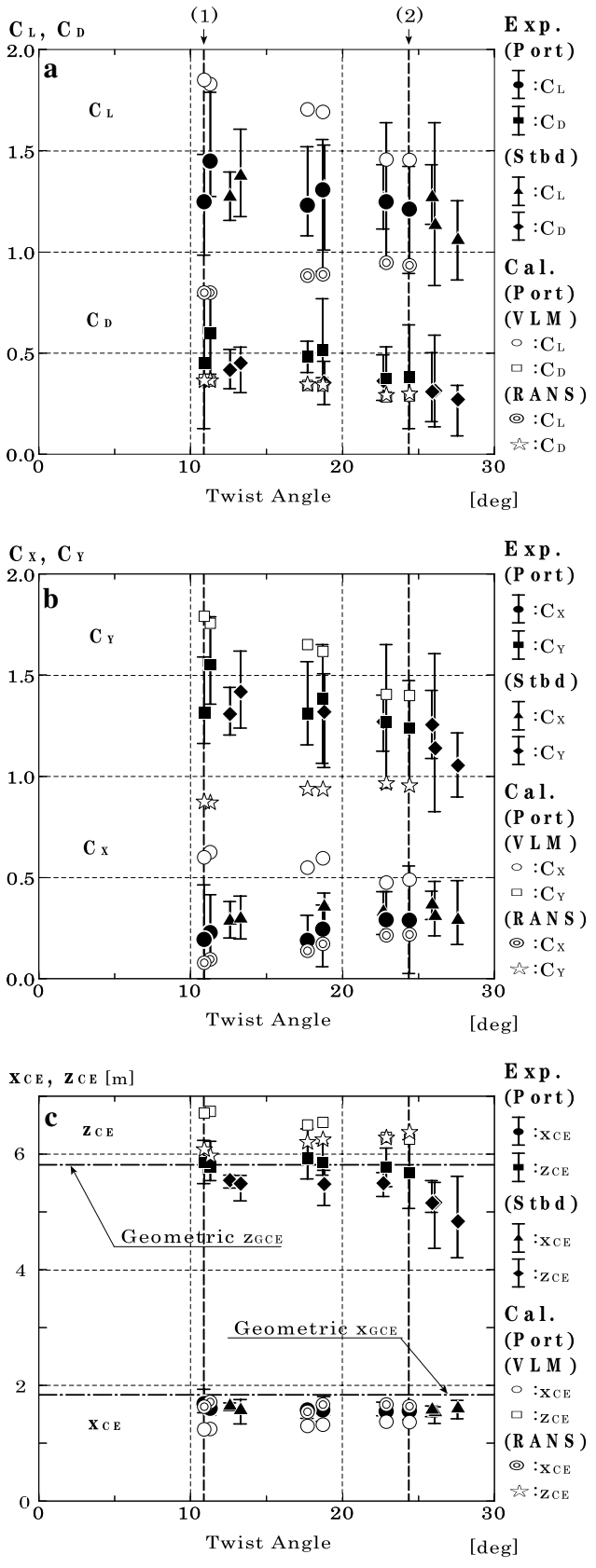

Fig. 17 Performance variation as a function of mainsail twist angle for mainsail alone. **a** C_L, C_D; **b** C_X, C_Y; **c** x_{CE}, z_{CE}

suction side of the mainsail for the smaller twist angle show considerable flow separation. This is caused by the large angle of attack at the upper part of the sail due to the small twist angle. In contrast, for the larger twist angle shown in Fig. 14(2), there is a low negative pressure area at the luff on the suction side of the mainsail due to the small angle of attack. This is what causes the considerable reduction in the calculated value for C_X in Fig. 13b. Table 5 shows the shapes and three-dimensional coordinates of the sails for cases 1 and 2, which correspond to the calculated results shown in Fig. 14.

5.2 Mainsail with 75% jib

5.2.1 Variation with apparent wind angle

Figure 15 shows the performance variation for the mainsail and 75% jib configuration as a function of AWA. Unfortunately, the longitudinal position of the jib rail track was located slightly aft of the correct position for the 75% jib. Hence the upper part of the sail was not trimmed adequately. This caused the gradual variation of C_L in Fig. 15a as a function of AWA, compared to Fig. 9a. It should be noted that the sail area for the nondimensionalization in this case is 46.9 m^2, which is 79% of that of the mainsail with 130% jib configuration. Although the results for C_L using VLM increase with increasing AWA, the results using RANS-based CFD show good agreement with those from the experiment. However, the calculated C_D for an AWA of 28.3° (ID 98110108) is considerably higher than the experimental results. This discrepancy is likely to be due to the extreme suction-side flow separation predicted in the computational results. A possible reason for this is insufficient grid resolution and inadequate representation of the sail geometry in the computational grid, especially near the leading edge. RANS-based CFD may tend to be sensitive to the grid accuracy and overpredict flow separation, especially for larger values of AWA. This needs to be investigated further. In Fig. 15c, the x and z coordinates of GCE for this configuration are 0.85 m aft and 5.14 m above the origin, respectively. The experimental data are close to these values.

Figure 16 shows the calculated results using RANS-based CFD. Figure 16(1) corresponds to experimental ID 98110105 (AWA = 20.5°), and Fig. 16(2) corresponds to ID 9811032A (AWA = 35.2°). In both cases, it is seen that the streamlines at the upper part of the pressure side of the jib show considerable flow separation. This is caused by the negative angle of attack at the upper part due to the unsuitable jib sheet position. Table 6 shows the shapes and three-dimensional coordinates of the sails for cases 1 and 2, which correspond to the calculated results shown in Fig. 16.

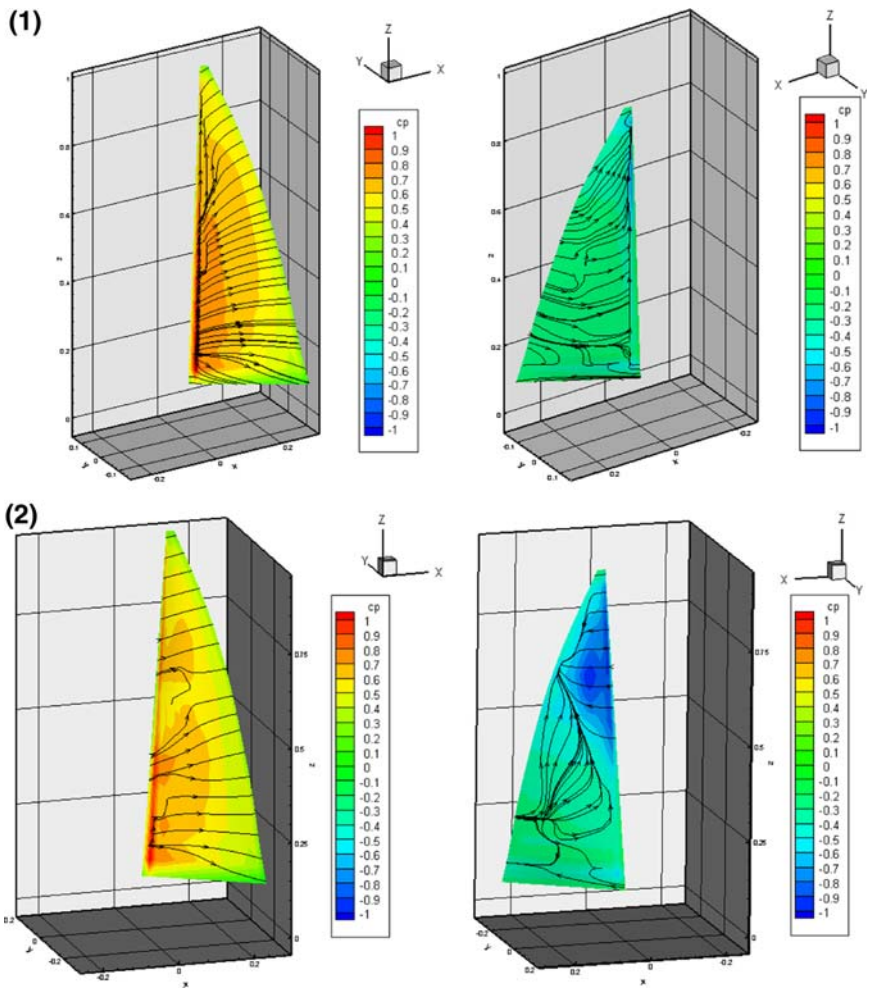

Fig. 18 (1) Surface pressure and streamlines obtained by RANS-based CFD for mainsail alone at experimental ID 9807172B (twist angle = 10.9°). (2) Surface pressure and streamlines obtained by RANS-based CFD at experimental ID 9807172F (twist angle = 24.4°)

5.3 Mainsail alone

5.3.1 Variation with mainsail twist angle

Figure 17 shows the performance variation for the mainsail alone as a function of the mainsail twist angle. The experiment was performed with an average value of AWA of 30° ± 2° and a mean draft of around 10%.

In the figure, the twist angle ranges from 10.9° to 24.4° for the port tack. Varying the twist angle by 13.5°, changes the value of C_X from 0.19 to 0.29 (53%) and the value of C_Y from 1.24 to 1.55 (25%). It should be noted that the sail area for the nondimensionalization in this case is 33.2 m^2, which is 56% of that of the mainsail with 130% jib configuration. In this case, since the true wind velocity was insufficient, the boat was given additional thrust using an auxiliary engine in order to obtain sufficient apparent wind speed. For the case of the mainsail and jib configuration, the sailing boat was steered by looking at the shape of the luff of the jib. Therefore, when there is no jib, it is difficult to steer adequately and the deviation in AWA becomes larger. This is the reason for the wider error bars than for the mainsail and jib configurations.

In the small twist angle range, the value of C_D exceeds 0.5. This might be caused by the generation of wide flow separation on the mainsail surface. Since the AWA and mainsail trim are almost the same as those used for the configuration with the mainsail and the 130% jib, this result clearly indicates the effect of the jib on decreasing the flow separation on the mainsail. In this case, the calculated results for C_L using VLM show higher values, as flow separation is not taken into account. In contrast, the results using RANS-based CFD significantly underpredict the experimental results. In Fig. 17c, the x and z coordinates of GCE for this configuration are 1.84 m aft and 5.82 m above the origin, respectively. The experimental data are close to these values.

Figure 18 shows the results calculated using RANS-based CFD. Figure 18(1) corresponds to experimental ID 9807172B (twist angle = 10.9°), and Fig. 18(2) corresponds to ID 9807172F (twist angle = 24.4°). It can be seen that the streamlines on the suction side indicate flow separation for both cases. In particular, in Fig. 18(1), the attack angle of the mainsail becomes 20°–30°. This causes more severe flow separation and a considerably lower

Table 7 Sail shapes, measured experimental data and three-dimensional coordinates of the sails for the cases of (1) 9807172B and (2) 9807172F

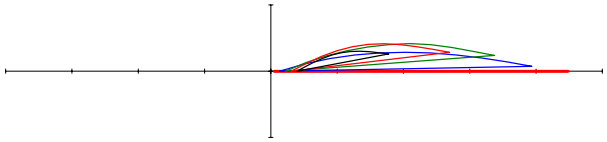

(1) 9807172B

AWA[deg]	TWIST[deg]	DRAFT[%]	AWS[m/s]	HEEL[deg]	VB [kt]
29.8	10.9	9.3	7.2	8.3	(4.2)
C_L	C_D	C_X	C_Y	x_{CE} [m]	z_{CE} [m]
1.25	0.45	0.19	1.31	1.68	5.86

% of heit	x	y	z	Mainsail x	Mainsail y	Mainsail z
0 %				0.046	0.000	1.320
				0.934	0.000	1.320
				1.822	0.000	1.320
				2.710	0.000	1.320
				3.598	0.000	1.320
				4.486	0.000	1.320
20 %				0.133	0.000	3.820
				0.891	0.190	3.820
				1.650	0.274	3.820
				2.411	0.274	3.820
				3.173	0.200	3.820
	Without Jib			3.937	0.072	3.820
40 %				0.221	0.000	6.320
				0.837	0.231	6.320
				1.461	0.364	6.320
				2.091	0.417	6.320
				2.730	0.357	6.320
				3.373	0.236	6.320
60 %				0.308	0.000	8.820
				0.765	0.223	8.820
				1.231	0.370	8.820
				1.710	0.414	8.820
				2.199	0.370	8.820
				2.693	0.284	8.820
80 %				0.396	0.000	11.320
				0.656	0.138	11.320
				0.923	0.244	11.320
				1.199	0.297	11.320
				1.487	0.293	11.320
				1.780	0.261	11.320
100 %				0.483	0.000	13.820
				0.512	0.009	13.820
				0.540	0.018	13.820
				0.569	0.025	13.820
				0.599	0.031	13.820
				0.628	0.038	13.820

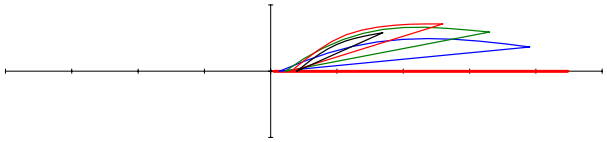

(2) 9807172F

AWA[deg]	TWIST[deg]	DRAFT[%]	AWS[m/s]	HEEL[deg]	VB [kt]
30.5	24.4	9.7	7.3	8.8	(5.3)
C_L	C_D	C_X	C_Y	x_{CE} [m]	z_{CE} [m]
1.21	0.38	0.29	1.24	1.56	5.67

% of heit	x	y	z	Mainsail x	Mainsail y	Mainsail z
0 %				0.046	0.000	1.320
				0.934	0.000	1.320
				1.822	0.000	1.320
				2.710	0.000	1.320
				3.598	0.000	1.320
				4.486	0.000	1.320
20 %				0.133	0.000	3.820
				0.869	0.276	3.820
				1.615	0.443	3.820
				2.372	0.492	3.820
				3.138	0.453	3.820
	Without Jib			3.908	0.365	3.820
40 %				0.221	0.000	6.320
				0.793	0.349	6.320
				1.389	0.569	6.320
				2.010	0.660	6.320
				2.651	0.648	6.320
				3.301	0.590	6.320
60 %				0.308	0.000	8.820
				0.712	0.315	8.820
				1.141	0.549	8.820
				1.607	0.664	8.820
				2.095	0.707	8.820
				2.595	0.712	8.820
80 %				0.396	0.000	11.320
				0.626	0.181	11.320
				0.867	0.338	11.320
				1.126	0.454	11.320
				1.405	0.527	11.320
				1.692	0.580	11.320
100 %				0.483	0.000	13.820
				0.508	0.016	13.820
				0.534	0.032	13.820
				0.560	0.047	13.820
				0.586	0.061	13.820
				0.613	0.075	13.820

value of C_L than that shown in Fig. 18(2). For large attack angles, the accurate prediction of the flow separation on the lifting surface is one of the big challenges for RANS-based CFD. This will be investigated further. Table 7 shows the shapes and three-dimensional coordinates of the sail for cases 1 and 2, which correspond to the calculated results shown in Fig. 18.

6 Discussion of RANS-based CFD

The flow is dominated by multiple-lifting-surface aerodynamic interactions. For larger AWA values, in particular, a large-scale flow separation exists on the leeward side of the sails. In general, there is complex vortex generation in the wake, especially near the top and bottom of the sails, i.e., tip vortices are generated and are influenced by the boundary layer flows on the sails. The resultant aerodynamic forces are mostly dominated by the pressure component, whereas the contribution of the frictional component is generally small. The accurate prediction of the boundary layer flows on the sails and the three-dimensional flow separation, associated with the above-mentioned vortex generation, are big challenges for RANS-based CFD. The geometrical complexity is also another significant challenge to RANS-based CFD. The

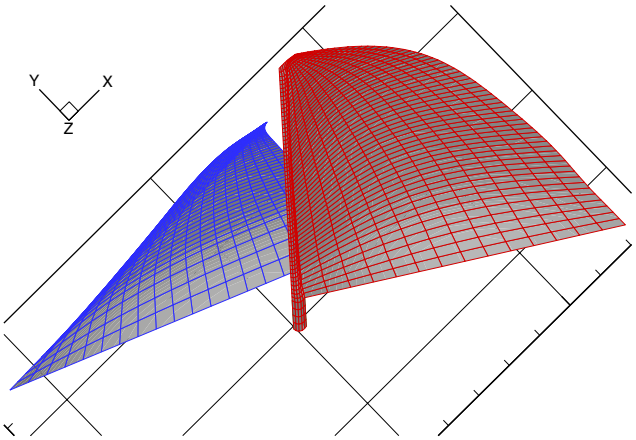

Fig. 19 Overview of sail surface grids including mast geometry. All surfaces are defined in Initial Graphics Exchange Specification (IGES) format

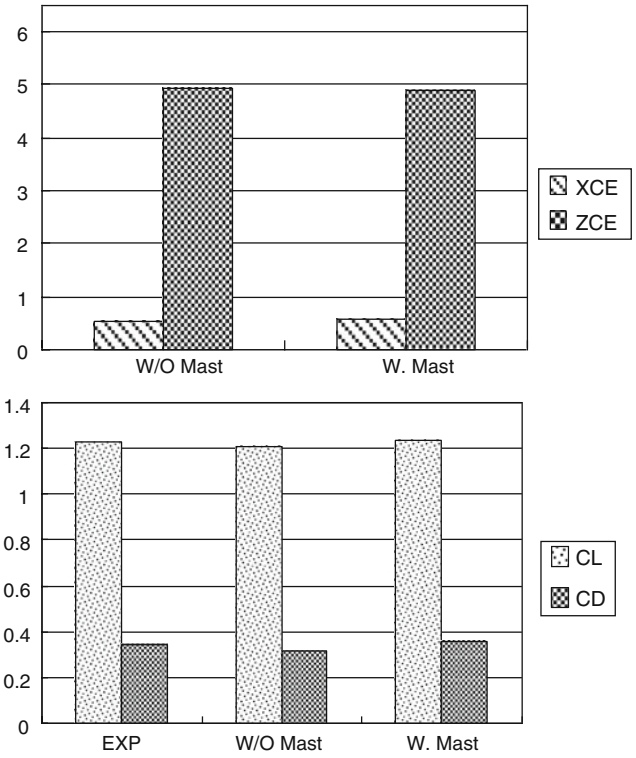

Fig. 20 Comparison of aerodynamic forces and center of effort (*CE*) with and without the mast (*W Mast*, with mast; *W/O Mast*, without mast)

accuracy in the prediction of the CE is of great interest, in association with the correct prediction of the above-mentioned three-dimensional flow separation.

Through the analyses of the results, it appears that the overall trends of the flow and the aerodynamic forces measured in the experiments are fairly well predicted by the present computations. It is also seen that the multi-block domain decomposition considered here is very effective for the present mainsail and jib configurations. The automatic gridding scheme used successfully generates high-quality structured grids for the various sail geometries, AWA, and heel angles considered in the present study. Although there are advantages to a structured grid system for high-resolution in the boundary layer flow, building a grid in this fashion is difficult to apply to complex geometries. This problem appears to be resolved by the present scheme.

7 Influence of the mast

The present RANS-based CFD method was applied to investigate the influence of the mast on the flow, and hence on the aerodynamic forces for AWA = 31.1°, heel angle = 12.3°, and Twist angle = 24.1°, i.e., experimental ID 97072218.

Figure 19 shows the computational geometries for the mainsail, jib, and mast configuration. For the present study, all the surface data are represented using the Initial Graphics Exchange Specification (IGES) format. Then, the data were used for multiblock grid generation by using the commercial software GRIDGEN v.15 (Pointwise, Fort Worth, TX, USA). Application of this software is very useful for investigating appropriate grid topology and resolution. In future work, the gridding procedure will be fully automated.

For the correct representation of the mast geometry, the number of computational grids and multiblocks needed to be slightly increased, i.e., around 700,000 grid points and 52 blocks were used. The grids for both the with-mast and without-mast cases were generated with careful consideration to minimizing the grid dependency of the results, so the same number of grids and blocks were used for the two cases. The overall grid quality was similar to that for the calculation series discussed above, which is supported by the fact that the differences in the x_{CE}, z_{CE}, C_L, and C_D values for the without-mast case between the present calculation and the series calculation were all less than 0.5%. Converged solutions were obtained within 2000 RANS global iterations, i.e., for a nondimensional time of 20. This is a similar convergence trend to that for the calculation series.

Figure 20 shows a comparison of CE and the aerodynamic forces for cases with and without a mast. In addition, Fig. 21 shows the pressure on the sail surface and the streamlines and Fig. 22 shows stream ribbons in the flow field to identify the salient influence of the mast on the flow

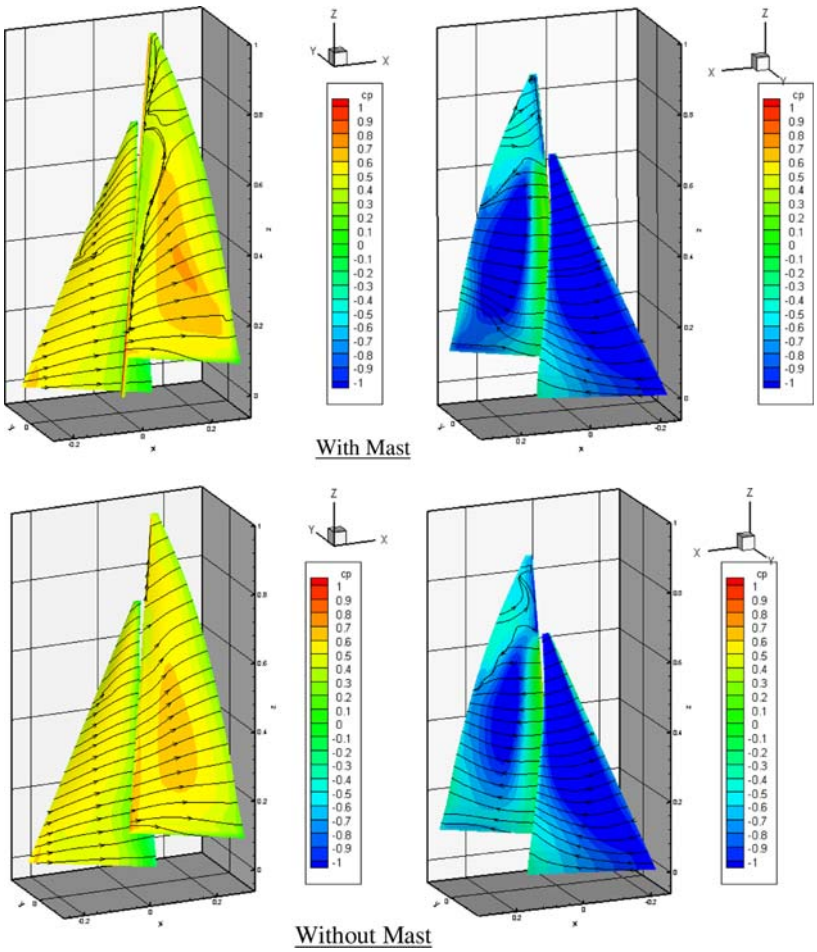

Fig. 21 Comparison of surface pressure and streamlines between with-mast (*upper*) and without-mast (*lower*) cases. *Left* and *right* columns correspond to the port and starboard sides, i.e., pressure and suction sides, respectively

by comparison of the two cases. The local flow field on the horizontal midsection of the mainsail is shown in Fig. 23. Note that the present computation simulates port-tack sailing, therefore, the port and starboard sides correspond to the pressure and suction sides, respectively.

It can be seen in the present results that the influence of the mast on flow is particularly significant in the mast-wake region. The limitation of the resolution of the present computational grid precludes detailed analysis of the vortex shedding that occurs on the mast surface, but the gross features of the influences of the mast on the downstream flow can be seen. The surface streamlines on the mainsail indicate complex three-dimensional separation in the mast-wake region, which is more obvious on the pressure side surface. Despite the redirection of the surface streamlines, the general features of the surface pressure distributions on the mainsail are similar to those for the without-mast case. The influence of the mast on the flow downstream is due to flow separation and vortex generation on the mast surface, which directly leads to an increase in drag force. The inclusion of the mast increases C_D by about 11%, and the resultant value is closer to the experimental data. The differences in C_L and z_{CE} between the with-mast and without-mast cases are less that 1% and these may be judged insignificant. x_{CE} is moved aft by about 10% by the presence of the mast, and the resultant value is closer to the measurements.

In summary, as far as the present sail configuration and sailing conditions are concerned, taking into account the presence of the mast in the calculations results in the predictions being closer to the experimental results. Including the mast is more realistic and will result in improved prediction of the flow and the aerodynamic forces. The special care required for constructing the computational grids may be a drawback; however, in the near future, increases in computing power will reduce limitations on grid size and permit further grid refinement to capture the more detailed flow structure behind the mast. Introduction of overset grid technology may also be of considerable benefit in overcoming this problem.

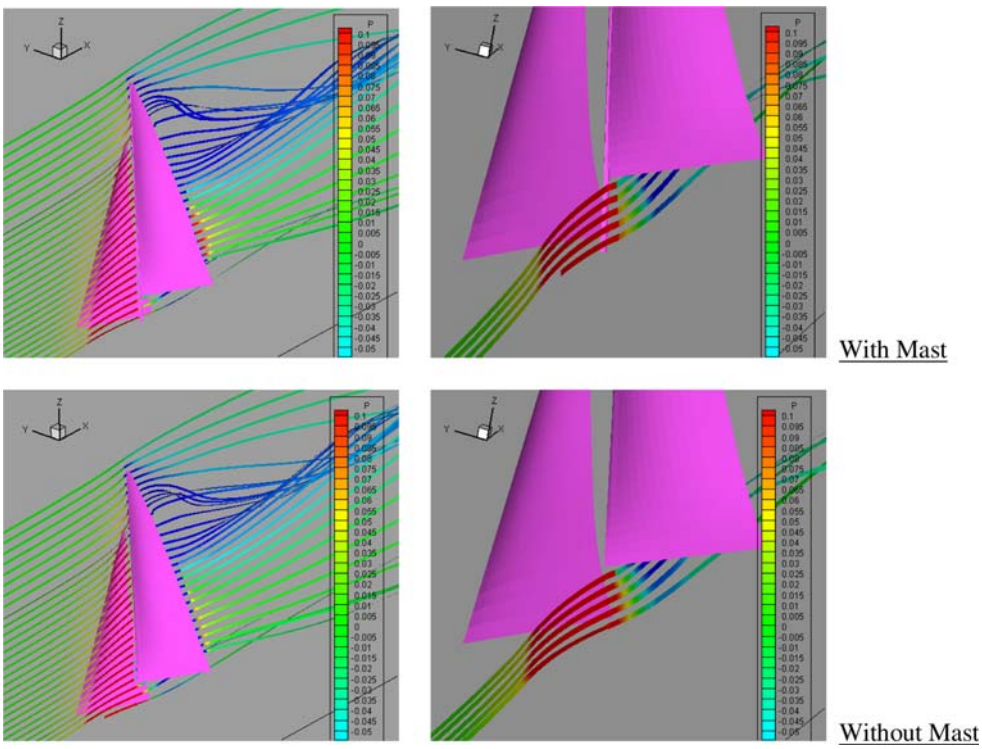

Fig. 22 Comparison of stream ribbons between with-mast (*upper*) and without-mast (*lower*) cases. *Left* and *right* graphics correspond to global and local views, respectively

8 Conclusions

The sail shapes and performance of IMS type sails were measured using the sail dynamometer boat *Fujin* for the upwind condition. The sail configurations tested were as follows: mainsail with 130% jib; mainsail with 75% jib; and mainsail alone. The three-dimensional coordinates of the sails were obtained from the measured data and tabulated with the aerodynamic coefficients.

Numerical calculations were also performed using the measured sail shapes. The calculation methods were of two types: Reynolds-Averaged Navier–Stokes (RANS)-based CFD and the vortex lattice method (VLM). A multi-block RANS-based CFD method developed by one of the authors was used together with an automatic grid generation scheme. The computed results were compared with the measured data.

From the experiments, the variation of sail performance (mainly the lift and drag coefficients and the coordinates of the center of effort) were measured quantitatively at full-scale as functions of AWA, mainsail mean draft, and mainsail twist angle. In particular, for the case of the mainsail and 130% jib configuration, it was clarified that the maximum thrust force coefficient C_X occurred at a mainsail mean draft of around 10–12% and at a mainsail twist angle of around 15°. These trends were well predicted by both numerical calculation methods. For the case of the mainsail alone, the calculated results did not correspond with the measured data. This might be caused by the large attack angle of the mainsail without a jib. The accurate prediction of the flow separation on the lifting surface at large attack angles is one of the big challenges for RANS-based CFD. This will be investigated further. Except for the case of the mainsail alone, it appears that the overall trends of the flow and the aerodynamic forces measured in the experiments are fairly well predicted by the present computations.

The RANS-based CFD method was also applied to investigate the influence of the mast on the flow and the aerodynamic forces. It was found that when the mast was included in the calculations, the value of C_D increased by about 11% and the resultant value was closer to the experimental data. Further grid refinement to capture the more detailed flow around mast and sails will be conducted in the near future. The sail shape database and the comparison with the numerical calculations indicated in this article provide a good benchmark for sail performance analysis of the upwind condition for IMS type sails.

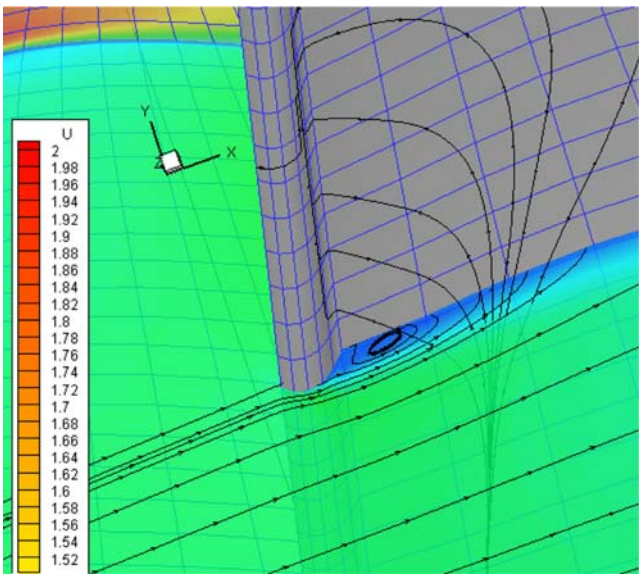

Fig. 23 Surface streamlines on mainsail and in horizontal cross section (z = 0.5, midsection of mainsail) for the with-mast case

Acknowledgments The sail dynamometer boat *Fujin* was built for sail tests for the Japanese America's Cup entry by a Grant-in-Aid from the Nippon Foundation and the authors would like to thank the Nippon Foundation for providing them this invaluable tool. The authors wish to express their thanks to Yamaha Motor Co. Ltd. for building *Fujin* and to North Sails Japan Co. for making the sails. We would like to thank Dr. Martin Renilson for his valuable discussions and comments on this article. We would also like to thank Mr. H. Mitsui, the harbormaster of the Anamizu Bay Seminar House of the Kanazawa Institute of Technology, for his assistance with the sea trials. Help with the sea trials given by graduate and undergraduate students of the Kanazawa Institute of Technology is also gratefully acknowledged. The graduate students were Masaya Miyagawa, Takashi Hasegawa, and Munehiko Ogihara.

References

1. Milgram JH, Peters DB, Eckhouse DN (1993) Modeling IACC sail forces by combining measurements with CFD. 11th Chesapeake sailing yacht symposium, SNAME, Annapolis
2. Masuyama Y, Fukasawa T, Kitasaki T (1997) Investigations on sail forces by full-scale measurement and numerical calculation (part 1: steady sailing performance). J Soc Naval Archit Jpn 181:1–13 (in Japanese)
3. Hochkirch K, Brandt H (1999) Fullscale hydrodynamic force measurement on the Berlin sailing dynamometer. In: 14th Chesapeake sailing yacht symposium, SNAME, Annapolis
4. Hansen H, Jackson P, Hochkirch K (2003) Comparison of wind tunnel and full-scale aerodynamic sail force. Int J Small Craft Technol (IJSCT) 145(Part B1):23–31
5. Krebber B, Hochkirch K (2006) Numerical investigation on the effects of trim for a yacht rig. 2nd High Performance Yacht Design Conference, RINA, Auckland, New Zealand
6. Masuyama Y, Fukasawa T (1997) Full-scale measurement of sail force and the validation of numerical calculation method. 13th Chesapeake sailing yacht symposium, SNAME, Annapolis
7. Fukasawa T (1993) Aeroelastic transient response of 3-dimensional flexible sail. Aero-hydroelasticity, developments and applications. In: Proceedings of international conference on aero-hydroelasticity, ICAHE'93, Beijing, China
8. Tahara Y (1996) A multi-domain method for calculating boundary-layer and wake flows around IACC sailing yacht. J Kansai Soc Naval Arch Jpn 226:63–76
9. Tahara Y (1996) Evaluation of a RANS equation method for calculating ship boundary layers and wakes including wave effects. J Soc Naval Archit Jpn 180:59–80
10. Tahara Y (1999) Wave influences on viscous flow around a ship in steady yaw motion. J Soc Naval Archit Jpn 186:157–168
11. Tahara Y, Ando J (2000) Comparison of CFD and EFD for KCS container ship in without- and with-propeller conditions. Gothenburg 2000—A workshop on numerical ship hydrodynamics, Gothenburg, Sweden
12. Tahara Y, Wilson R, Carrica P, Stern F (2006) RANS simulation of a container ship using a single-phase level set method with overset grids and prognosis for extension to self-propulsion simulator. J Mar Sci Technol 11(4):209–228
13. Tahara Y, Stern F, Himeno Y (2004) Computational fluid dynamics-based optimization of a surface combatant. J Ship Res 48(4):273–287
14. Tahara Y, Tohyama S, Katsui T (2006) CFD-based multi-objective optimization method for ship design. Int J Numer Methods Fluids 52:449–527
15. Tahara Y, Hayashi G (2003) Flow analyses around downwind-sail system of an IACC sailing boat by a multi-block NS/RaNS method. J Soc Naval Archit Jpn 194:1–12
16. Tahara Y (2006) Development and demonstration of simulation based design for parachute aerodynamic design. 7th International conference on hydrodynamics, Ischia, Italy